Submitted to ApJ.
Preprint typeset using LaTeX style emulateapj v. 08/13/06

CIRCUMBINARY MHD ACCRETION INTO INSPIRALING BINARY BLACK HOLES

Scott C. Noble[1], Bruno C. Mundim[1], Hiroyuki Nakano[1], Julian H. Krolik[2], Manuela Campanelli[1], Yosef Zlochower[1], Nicolás Yunes[3]

[1] Center for Computational Relativity and Gravitation, Rochester Institute of Technology, Rochester, NY 14623
[2] Physics and Astronomy Department, Johns Hopkins University, Baltimore, MD 21218 and
[3] Department of Physics, Montana State University, Bozeman, MT 59717

Submitted to ApJ.

ABSTRACT

As two black holes bound to each other in a close binary approach merger their inspiral time eventually becomes shorter than the characteristic inflow time of surrounding orbiting matter. Using an innovative technique in which we represent the changing spacetime in the region occupied by the orbiting matter with a 2.5PN approximation and the binary orbital evolution with 3.5PN, we have simulated the MHD evolution of a circumbinary disk surrounding an equal-mass non-spinning binary. Prior to the beginning of the inspiral, the structure of the circumbinary disk is predicted well by extrapolation from Newtonian results. The binary opens a low-density gap whose radius is roughly two binary separations, and matter piles up at the outer edge of this gap as inflow is retarded by torques exerted by the binary; nonetheless, the accretion rate is diminished relative to its value at larger radius by only about a factor of 2. During inspiral, the inner edge of the disk at first moves inward in coordination with the shrinking binary, but as the orbital evolution accelerates, the rate at which the inner edge moves toward smaller radii falls behind the rate of binary compression. In this stage, the rate of angular momentum transfer from the binary to the disk slows substantially, but the net accretion rate decreases by only 10–20%. When the binary separation is tens of gravitational radii, the rest-mass efficiency of disk radiation is a few percent, suggesting that supermassive binary black holes in galactic nuclei could be very luminous at this stage of their evolution. If the luminosity were optically thin, it would be modulated at a frequency that is a beat between the orbital frequency of the disk's surface density maximum and the binary orbital frequency. However, a disk with sufficient surface density to be luminous should also be optically thick; as a result, the periodic modulation may be suppressed.

Subject headings: Black hole physics - magnetohydrodynamics - accretion, accretion disks - Galaxies: nuclei

1. INTRODUCTION

There is now excellent evidence that every galaxy with a bulge contains a supermassive black hole at its center (Gültekin et al. 2009). In addition, the prevailing theory of galaxy formation posits that today's massive galaxies were assembled from smaller pieces, as dark-matter haloes of progressively greater size merged (Davis et al. 1985; Bardeen et al. 1986). If massive black holes were already present in those progenitors, they would bring their black holes with them into the new combined galaxy, creating an opportunity for the black holes to merge. Such an event would be very exciting to detect for many reasons: It would reveal the presence of supermassive black holes early in the life of galaxies. It would shed important light on the growth of the strong correlations between nuclear black hole mass and galaxy structure (Gültekin et al. 2009). Most of all, it would provide a concrete example of one of general relativity's most spectacular predictions and possibly also allow a test of the validity of general relativity in a truly strong-field regime.

An extremely large amount of energy is very rapidly released in a binary black hole (BBH) merger event, almost all of it through gravitational radiation [several percent of the black hole masses in a timescale of $\sim (M_{\rm BBH}/M_\odot) \times 493\,\mu$s]. Gravitational radiation may be strong enough to eject the final remnant from its host galaxy, with recoil velocities or "kicks" up to $\approx 10^3$ km/s predicted by numerical relativity simulations (Baker et al. 2007; Campanelli et al. 2007a,b; González et al. 2007; Herrmann et al. 2007; Koppitz et al. 2007; Baker et al. 2008; Healy et al. 2009; Lousto et al. 2010; Lousto & Zlochower 2011; Lousto et al. 2012). Unfortunately, a gravitational wave observatory with adequate sensitivity in the appropriate frequency range is still well in the future, whether it operates by direct detection or through pulsar timing (Jennrich 2009; Wen et al. 2011). On the other hand, even if only a small part of the energy is deposited in nearby gas, the associated photon signals might be much more readily seen with instruments operating today. Because the energy given to the gas comes from work done by gravitational forces, one would expect, on the basis of the Equivalence Principle, that the total energy added to the gas would be proportional to its mass. If most of this added energy is dissipated into heat (local irregularities are likely to drive shocks), the total energy radiated in photons would then be similarly proportional to the gas mass (Krolik 2010). The question is, therefore: "How much mass would one expect in the neighborhood of a black hole merger?"

Even if a BBH were supplied with mass at a rate characteristic of high luminosity quasars ($\sim 10 M_\odot\,{\rm yr}^{-1}$), several effects may severely reduce how much gas remains

Electronic address: scn@astro.rit.edu

close to the binary. Torques exerted by the binary on the inflowing gas may hold back the inflow, preventing much of it from approaching closer than a few times the binary separation a (Pringle 1991; MacFadyen & Milosavljević 2008). As the binary compresses, whether by interactions with passing stars and external gas or by gravitational radiation, the gas follows, but is held off at a distance of at least $\simeq 2a$. Toward the end of the binary's evolution, gravitational radiation losses grow rapidly and dominate the orbital shrinkage. Ultimately, the orbit shrinks on a timescale shorter than the characteristic accretion inflow time and the BBH is expected to decouple from the disk. After such decoupling, there would not be enough time for much disk mass to catch up with the black holes before they merge (Milosavljević & Phinney 2005). Thus, for a given external supply rate, the amount of gas available to be heated in a merger is determined by a competition between the internal stresses that drive inflow and a pair of dynamical mechanisms that tend to keep gas at "arms-length" from the merging black holes.

Until recently, efforts to quantify these effects have relied almost entirely on the phenomenological Shakura-Sunyaev α-disk model to describe internal stresses (Milosavljević & Phinney 2005; MacFadyen & Milosavljević 2008; Liu & Shapiro 2010; Tanaka & Menou 2010), in which the vertically-integrated and time- and azimuthally-averaged internal stress is supposed to be a factor α times the similarly integrated and averaged pressure; the only exceptions were studies focusing on binaries with large mass ratios between primary and secondary, a limit primarily relevant to planet formation and to extreme-mass ratio inspiral sources (Winters et al. 2003; Papaloizou & Nelson 2003; Nelson & Papaloizou 2003; Kocsis et al. 2011; Yunes et al. 2011). Moreover, with the exception of Farris et al. (2011) and Bode et al. (2012), which assumed these stresses were negligible, all these calculations also assumed Newtonian dynamics. However, there is strong reason to think that the actual mechanism of these stresses is magnetohydrodynamic (MHD) turbulence, stirred by the magnetorotational instability (MRI) (Balbus & Hawley 1998). In contrast to ordinary, isotropic turbulence, orbital shear makes this turbulence highly anisotropic, so that there is a non-zero correlation between the radial and azimuthal components of the magnetic field; this correlation creates the stress. MHD calculations are therefore required, at the very least, to establish the appropriate scale of the stresses and the approximate magnitude of α. In addition, although the α-model may give a reasonable description of time-averaged behavior well inside the body of an accretion flow, it is particularly ill-suited for predicting dynamical behavior on shorter timescales (Hirose et al. 2009) and at disk edges (Krolik et al. 2005; Noble et al. 2010). Because the key issues in how much gas reaches a merging BBH depend, of course, on the time-dependent behavior of gas near and within the inner edge of a disk, explicit calculation of the MHD turbulence is also required for an accurate treatment of the time- and spatial-dependence of the internal stress.

In this paper, we present the first simulation of a circumbinary accretion disk around a binary black hole system during the epoch in which the binary's inspiral time grows shorter than the inflow time through the disk. Generically, this period occurs not long before the binary's final merger. Our physics treatment includes fully relativistic MHD. This study differs from that of Shi et al. (2011), who presented similar MHD simulations, but concentrated on the Newtonian regime, when the black holes are very widely separated. Moreover, their Newtonian treatment did not allow for the black holes to inspiral, a reasonable assumption when the semi-major axis is hundreds of thousands of gravitational radii, but a terrible assumption in the late inspiral. We here focus on BBHs with separations of $\sim (10\text{–}20)\, r_g$, where $r_g \equiv GM/c^2$ and M is the total mass of the binary (we adopt geometric units with $G = c = 1$ for the remainder of this paper). The spacetime associated with the BBH orbital dynamics is described through a vacuum post-Newtonian (PN) approximation (see the review paper of Blanchet (2002) and references therein), where we neglect the back reaction of the disk on the BBH dynamics. Our work also contrasts with that of Giacomazzo et al. (2012), who employed full numerical relativity to compute the spacetime in which an initially uniform gas distribution with an externally-imposed uniform magnetic field evolved during the last 3 orbits before merger.

As we will describe below, the PN approximation is adequate to describe the spacetime evolution for our needs. The PN scheme is a method to describe approximately the dynamics of physical systems in which motions are slow compared to the speed of light and gravitational fields are weak. That is, one solves the Einstein field equations perturbatively, expanding in $(v/c)^2 \ll 1$ and $r_g/r = GM/(rc^2) \ll 1$ Here v, M and r are the characteristic velocity, mass and size or separation of the system. This approximation has been remarkably effective in describing the perihelion precession of Mercury Einstein (1915), and the gravitational-wave loss from binary systems, such as the Hulse-Taylor pulsar, PSR B1913+16 (see e.g. Weisberg & Taylor (2005); Will (2011)). PN theory also plays a key role in the construction of the gravitational-waveform templates (Sathyaprakash & Schutz 2009) for inspiraling compact objects currently used in the search for gravitational waves by laser-interferometric observatories. PN theory has also been recently interfaced with numerical relativity simulations to serve as initial data for the modeling of BBH mergers (Tichy et al. 2003; Bonning et al. 2003; Yunes et al. 2006; Yunes & Tichy 2006; Yunes 2007; Kelly et al. 2007; Campanelli et al. 2009; Johnson-McDaniel et al. 2009; Kelly et al. 2010; Mundim et al. 2011). In all cases, the PN approximation is developed to sufficiently high perturbative order that the error contained in the approximation is much smaller than that associated with either the data in hand (in the case of binary pulsars) or the data expected (in the case of direct gravitational wave detection).

Using this PN-approximated description of the spacetime, we first evolve the BBH at a fixed initial separation $a_0 = 20M$ to allow the accretion disk to relax to a quasi-steady state. To study the effect of orbital shrinkage on the accretion disk, we then follow the binary inspiral until it reaches a separation $a = 8M$, beyond which the PN approximation ceases to be sufficiently accurate for our purposes. In a separate simulation, we kept the binary's

separation fixed at $20M$ and continued to evolve until $\simeq 76000M$ to study the secular dynamics of the quasi-steady state, and, by contrasting with the first simulation, highlight the special effects induced by the inspiral.

Our findings can be summarized as follows. The mass at $r \simeq 2.5a$ builds steadily throughout the quasi-steady state, but much of it eventually concentrates in a distinct "lump". At smaller radii, a gap is cleared as torques and forces exerted by the binary either sweep matter inward or fling it outward. Much of the small amount of mass in this gap is found in a pair of streams emanating from the inner edge of the disk and curving inward toward each black hole. These streams carry nearly half of the mass accreting through the bulk of the disk to the inner boundary of the problem volume at $r = 0.75a_0$.

As the binary starts to shrink, the inner edge of the disk at first moves inward following the orbital evolution of the binary, but eventually cannot keep up, as the orbital shrinkage grows faster. Nevertheless, a significant amount of mass still follows the binary's inspiral within the gap region. We find that the final accretion rate in the inspiral stage is about 70% of the corresponding rate in the steady-state stage.

The luminosity of the disk is proportional to its surface density. If the accretion rate fed to the disk were comparable to that of ordinary AGN, the surface density, and therefore the luminosity, of such a circumbinary disk could approach AGN level. Most strikingly, the luminosity should be modulated periodically at a frequency determined by the binary orbital frequency and the binary mass ratio—1.46 times the binary orbital frequency in the case of equal masses. However, the amplitude of modulation may be reduced by the large optical depth of the disk if the surface density is large enough to generate a sizable luminosity.

This paper is organized as follows. In Section 2 we describe the construction of the dynamical BBH spacetime. In Section 3, we report the details of the MHD simulations of the disk. In Section 4 and Section 5, we present the results from these simulations and interpret them in the light of previous work and from the point of view of potential observational signatures. Finally, in Section 6, we summarize our principal conclusions.

2. BINARY BLACK-HOLE SPACETIME

While solutions of the Einstein equations for single black holes were discovered as early as 1916 (Schwarzschild 1916), no exact closed-form solution to the two-body problem exists and one generally needs to solve the Einstein equation numerically. With the breakthroughs in numerical relativity (Pretorius 2005; Campanelli et al. 2006; Baker et al. 2006; Scheel et al. 2006), it is now possible to perform stable and accurate full numerical simulations of BBHs in vacuum for a wide variety of mass ratios and spins parameters. However, because the Einstein equations can be thought of as modified wave equations, with wave speeds of c, the Courant condition[1] greatly limits the timestep size, making full numerical simulations impractical when the characteristic MHD speeds are significantly smaller than c. On the other hand, if an approximate, but accurate, spacetime is given, the Courant condition is set by the MHD speeds, allowing for a much larger timestep. Fortunately, analytic perturbative techniques have been successfully developed to tackle the spacetime problem both in the regime where the black holes are not too close, as well as in the *close limit* regime where the spacetime can be treated as a perturbed single black hole. In this paper, we use the PN approach to model the spacetime of an inspiraling binary system prior to merger, neglecting the effect of the disk on the evolution of the black holes, from orbital separations of $20M$ down to $\sim 8M$, roughly where the standard PN approximation becomes inaccurate for our purposes.

Using this PN-approximated solution, we then solve for the relativistic MHD evolution of the circumbinary accretion disk. We stop the PN evolution at $r = 8M$, but one can in principle continue the simulations beyond this regime. To do so, one could use a snapshot of the PN metric and MHD data at that radius as initial conditions to then carry out a fully non-linear GRMHD evolution, using numerical relativity techniques to solve the coupled GRMHD Einstein system of equations (which will be the subject of an upcoming paper).

We perform two simulations: (i) RunSS keeps the semi-major axis of the binary artificially fixed at $20M$; (ii) RunIn starts from a snapshot of RunSS at $t = 40000\,M$ (or after $\simeq 70$ orbits) and then lets the black holes inspiral at the PN-theory prescribed rate down to a separation of $\sim 8M$. RunSS is used to study the secular evolution of the accretion disk at fixed binary separation, while RunIn is used to investigate how the diminishing separation alters this secular evolution. We describe our PN approach to model the spacetime metric below.

2.1. *The post-Newtonian Approximation*

The PN approximation is based on a perturbative expansion of all fields, assuming slow motion $v/c \ll 1$ and weak fields $GM/(rc^2) \ll 1$[2]. These assumptions allow us to search for solutions that can be expressed as a divergent asymptotic series about a flat Minkowski background spacetime. These perturbations obey differential equations determined by the PN-expanded Einstein field equations. One then solves such equations perturbatively and iteratively to construct an approximate solution.

The two body problem in the slow-motion/weak-field limit is better understood by classifying the spacetime into different regions, where different assumptions hold and different approximations can be used (see e.g. Thorne (1980); Alvi (2000, 2003); Yunes et al. (2006); Yunes & Tichy (2006); Yunes (2007); Johnson-McDaniel et al. (2009) for a review). Here we concentrate on the *near zone*, which is the region sufficiently far from the horizons that the weak-field approximation of PN is valid, but less than a reduced gravitational wave wavelength $\lambdabar$ away from the center of mass of the system, so that retardation effects can be treated perturbatively. We note that in the *far zone*, i.e. the radiation zone where retardation effects can no longer be treated perturbatively, a multipolar post-Minkowskian expansion can be used rather than a PN one. Very close

[1] The Courant condition is a stability condition relating the timestep dt to the spatial resolution h. The timestep is limited by $dt < h/v$, where v is the fastest propagation speed in the system of interest.

[2] Note that we have explicitly re-introduced c and G in this section in order to discuss the PN approximation.

to each black hole (i.e. in the *inner zone*), perturbed Schwarzschild solutions are used (which can be extended to include spin by using perturbed Kerr solutions). In this paper, the binary black hole metric will be approximated with only the near zone solution.

The PN approximation, of course, has its limits: binary systems eventually become so closely separated that a slow-motion/weak-field description is inappropriate. For example, consider the simple case of a test particle spiraling into a non-spinning (Schwarzschild) black hole in a quasi-circular orbit. Eventually, the particle will reach the innermost stable circular orbit, at which point its orbital velocity $v/c \sim 0.41$. Clearly, such a velocity is not much less than unity, and thus, the PN approximation need not be an accurate description of the relativistic orbital dynamics. Similarly, when comparable-mass BBHs inspiral, they eventually reach a separation at which the PN approximation is a bad predictor of the dynamics, since the small-velocity/weak-field assumptions are violated.

The determination of the formal region of validity of the PN approximation is crucial, but it can only be assessed when one possesses a more accurate, perhaps numerical, description of the orbital dynamics. This is indeed the case when considering extreme mass-ratio inspirals (EMRIs), consisting of a stellar-mass compact object spiraling into a supermassive black hole. When considering EMRIs, one can model the spacetime through black hole perturbation theory, i.e., by decomposing the full metric as that of the supermassive black hole plus a perturbation induced by the stellar-mass compact object, without assuming slow motions (see e.g. Section 4 of Hughes (2009) for a recent review, Mino et al. (1997); Sasaki & Tagoshi (2003); Barack (2009); Poisson et al. (2011) for related topics). To leading-order, the orbital dynamics are then described by geodesics of the small object in the spacetime of the supermassive black hole. The orbital motions are slowly perturbed by the radiation reaction due to the emission of gravitational waves.

The comparison of black hole perturbation theory and PN theory predictions has allowed for the construction of different measures to estimate the PN region of validity. When considering the reduction in signal-to-noise ratio induced by filtering an "exact" black-hole perturbation theory gravitational wave with a 4PN[3] order filter, Poisson (1995) found that PN theory is sufficiently accurate provided $v \lesssim 0.2$. When considering the 5.5 and 4PN order predictions for the loss of the binary's binding energy for non-spinning and spinning background black holes respectively, relative to an "exact" black hole perturbation theory prediction, Yunes & Berti (2008) and Zhang et al. (2011) found that the former is accurate provided $v \lesssim 0.29$, which corresponds to an orbital separation of $a \gtrsim 11M$. The difference between these estimates is due to the different measures used and the different order of the PN approximation employed[4].

The region of validity of the PN approximation for comparable-mass binaries has not been as well studied. This is because black hole perturbation theory is not applicable here, and one must rely on full numerical relativistic simulations. Currently, state-of-the-art simulations can only model the last few tens of orbits prior to merger, while the determination of the formal region of validity would require knowledge of at least the last thousand orbits. Nonetheless, there exist analytical arguments suggesting that the region of validity in the comparable-mass case is larger than in the EMRI case (i.e., the PN expansion is valid for even larger velocities) (Simone et al. 1997; Blanchet 2003; Mora & Will 2004). Moreover, the NINJA (Numerical INJection Analysis)-2 project (Ajith et al. 2012), a collaboration between numerical relativists and gravitational wave data analysts, has established that certain 3PN order gravitational waveforms are sufficiently accurate for use as templates provided $v \lesssim 0.33$ ($a \gtrsim 8M$).

2.2. *Near-Zone PN Evolution*

The PN order of a given term is determined by the exponent of the perturbation parameter contained in that term. In the near zone, the PN expansion of a BBH spacetime metric is a series expansion in the orbital velocity $v/c \ll 1$ and the field strength $GM_A/(r_A c^2)$, where M_A and r_A are the masses of the Ath particle and the distances from the Ath particle to a field point respectively. Here, we may consider $1/c$ as the PN parameter which goes to zero in the Newtonian limit $c \to \infty$. Notice that by the virial theorem $v^2/c^2 = \mathcal{O}[GM/(a\,c^2)]$. A term proportional to $(1/c)^n$ beyond the Newtonian (leading-order) expression is said to be of $(n/2)^{\text{th}}$ PN order.

The near zone metric will be described here by a resummed PN expression. One begins with the 2.5PN expansion of the metric for non-spinning point particles in a quasi-circular orbit in harmonic coordinates, given for example in Blanchet et al. (1998). Such a metric, however, describes black holes as point-particles, which is why one then applies a "background resummation", as in Yunes & Tichy (2006); Yunes (2007); Johnson-McDaniel et al. (2009). This resummation is intended to improve the strong-field behavior of the metric close to each point-particle, i.e., it recovers the horizon of each individual black hole. The metric can then be formally written as

$$g_{\mu\nu}(t,\,\vec{x}) = g_{\mu\nu}[\vec{x};\,\vec{y}_A(t),\,\vec{v}_A(t)]\,, \tag{1}$$

where $\vec{x}$ is a spatial vector from the binary's center of mass to a field point, while $\vec{y}_A(t)$ and $\vec{v}_A(t)$ are the particle's spatial location and 3-velocity with $A = (1,\,2)$. This metric depends on the mass of each individual black hole, but also on the binary orbital evolution $\{\vec{y}_A(t),\,\vec{v}_A(t)\}$ that must be prescribed separately. We will use Greek letters (e.g., μ, ν, λ, κ) to represent spacetime indices [0, 1, 2, 3], and Roman letters (e.g., i, j, k, l) to represent spatial indices [1, 2, 3].

The orbital evolution can also be prescribed within the PN approximation. We simplify the analysis by considering only quasi-circular orbits. This simplification is justified because gravitational wave emission tends to circularize binaries very efficiently, as demonstrated in the weak (Peters 1964) and strong field

[3] This was extended to 5.5PN order in the erratum and addendum of Poisson (1995).

[4] It is not surprising that beyond 3PN order the region of validity of the PN approximation shrinks. This is a property of divergent asymptotic series, whose behavior in the context of PN theory was analyzed by Yunes & Berti (2008) and Zhang et al. (2011).

regimes (Sperhake et al. 2008; Hinder et al. 2008, 2010). We will here use a 3.5PN expansion for the orbital phase evolution $\phi(t)$, as given for example by Equation (234) of Blanchet (2002), which depends on the quantity $\Theta = \nu(t_c - t)/(5M)$, where t is time, t_c is the time of coalescence, M is the total mass and $\nu = M_1 M_2/M^2$ is the symmetric mass ratio. The PN orbital freque calculated from $\Omega_{\rm bin} = d\phi/dt$ in this paper.

Although waveforms can be fully characterized b monics of the orbital phase, the latter depend c orbital trajectories. One may model these in har coordinates via

$$y_1^i(t) = \frac{M_2}{M} a(t) \left[\cos\phi(t),\, \sin\phi(t),\, 0\right] ,$$
$$y_2^i(t) = -\frac{M_1}{M} a(t) \left[\cos\phi(t),\, \sin\phi(t),\, 0\right] ,$$

where $a(t) = |\vec{y}_1(t) - \vec{y}_2(t)|$ is the orbital separat a function of time. This separation can be calc via the balance law (see e.g., (Blanchet 2002)), states that the local rate of change of the binary's c binding energy is exactly balanced by the gravita wave luminosity carried out to future null infinit into black hole horizons, namely

$$\frac{dE_{\rm Orb}}{dt} = -\mathcal{L}\,.$$

The rate of change of the orbital separation is then by

$$\frac{da}{dt} = -\left(\frac{dE_{\rm Orb}}{da}\right)^{-1} \mathcal{L}\,.$$

Assuming the initial condition $a(t=0) = a_0$, we find

$$t = t_c - \int_0^a da' \left(\frac{dE_{\rm Orb}}{da'}\right) \mathcal{L}^{-1}\,,$$

where the integrand is expanded in a Taylor PN and the coalescence time t_c is defined by

$$t_c = \int_0^{a_0} da \left(\frac{dE_{\rm Orb}}{da}\right) \mathcal{L}^{-1}\,. \qquad (7)$$

In this paper, we only use the part of $\mathcal{L}$ that is carried to future null infinity and, although Equations (6,7) are typically Taylor expanded to evaluate $t(a)$, here they are inverted through Newton-Raphson minimization to yield $a(t)$.

Given the above analysis, we can now calculate the time of coalescence and the number of orbits in each of the simulations carried out. As already discussed, RunSS is artificially kept at a fixed semi-major axis, so $a(t) = a_0$ for all times, and thus, formally $t_c = \infty$. On the other hand, RunIn keeps $a(t)$ fixed to $a(t) = a_0 = 20M$ for $t < t_{\rm shrink} \equiv 40000M$, after which it is allowed to evolve according to the PN equations of motion. The time of coalescence for this run can be computed by inverting Equation (6) to obtain $t_c \sim 14000M$, although to leading order it is approximately described by (Peters 1964)

$$t_c \sim \frac{5}{256\nu}\left(\frac{a_0}{M}\right)^4 M = \frac{5}{256}\left(\frac{a_0}{M}\right)^4 \frac{(1+q)^2}{q} M\,, \qquad (8)$$

where $q = M_2/M_1$ is the binary mass ratio. A BBH clearly takes longer to merge for systems that start at larger initial separations and that possess extreme mass ratios. Obviously, t_c is always defined as the length of time to coalesce, when the binary is allowed to inspiral. The total simulation time of RunIn is then $t_c + t_{\rm shrink} \sim 54000M$.

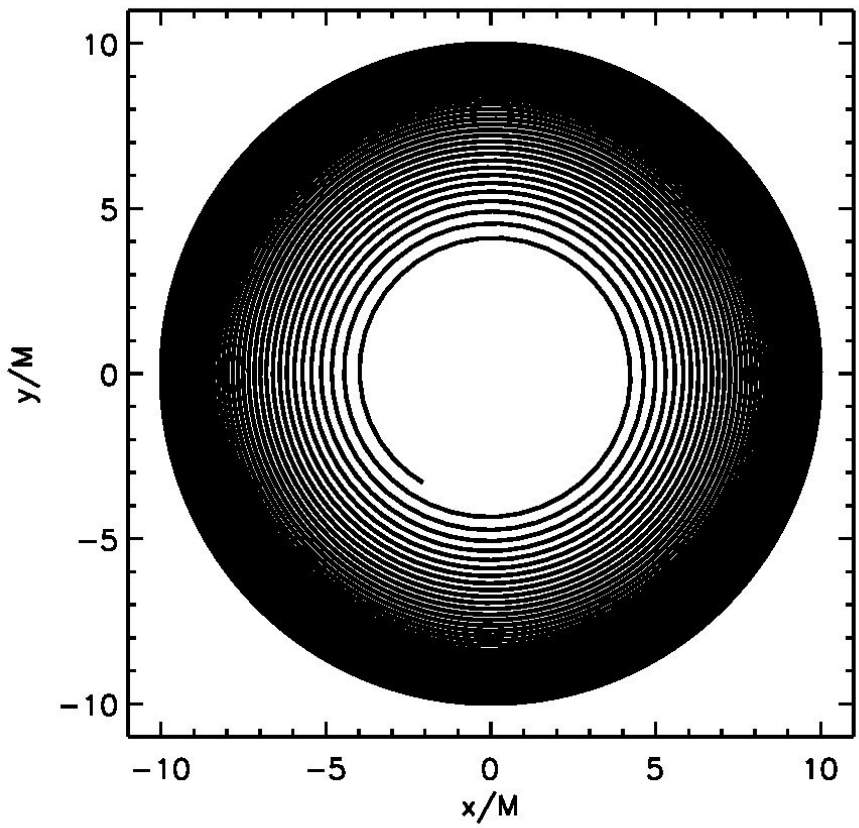

FIG. 1.— The orbital motion of one of the black holes in the binary from RunIn . Its trajectory starts from an initial separation of $a(0) = 20M$ and stops at $a(t_f) \simeq 8M$. Its black hole companion is located at a parity-symmetric point across the origin (track not drawn in the figure for the sake of clarity).

We have plotted a few diagnostics to get a sense of the evolution of the binary system in RunIn . Figure 1 shows the orbital evolution of the binary in the x-y plane, after it is allowed to inspiral. Figure 2 plots the orbital separation as a function of time. Observe that initially the semi-major axis is artificially kept fixed, while after $t > t_{\rm shrink}$ it is allowed to decrease due to gravitational radiation reaction. Figure 3 plots the number of orbits $N_{\rm orbits}$ traced by the binary system as a function of time, which is given by

$$N_{\rm orbits} = \begin{cases} \dfrac{1}{2\pi}\,\Omega_{\rm bin,0}\, t \;\; (\text{if } t < t_{\rm shrink})\,, \\ \dfrac{1}{2\pi}\,\left[\Omega_{\rm bin,0}\, t_{\rm shrink} + \phi(t - t_{\rm shrink})\right] \;\; (\text{if } t \geq t_{\rm shrink})\,. \end{cases} \qquad (9)$$

We have here defined $\Omega_{\rm bin,0} = \Omega_{\rm bin}(r = a_0)$ to be the (constant) PN orbital frequency at a fixed semi-major axis, and we have set $\phi(0) = 0$ for the PN phase evolution. The number of orbits is obviously a piece-wise function since when $t < t_{\rm shrink}$, $N_{\rm orbits}$ increases linearly,

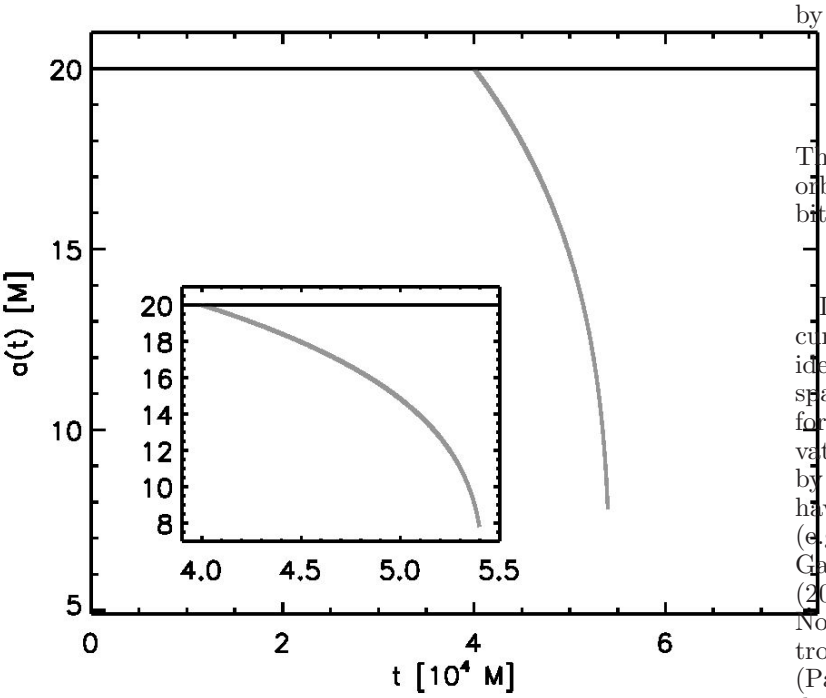

FIG. 2.— The evolution of the orbital separation with respect to time, $a(t)$. We turn on the gravitational radiation reaction at $t = 40000M$.

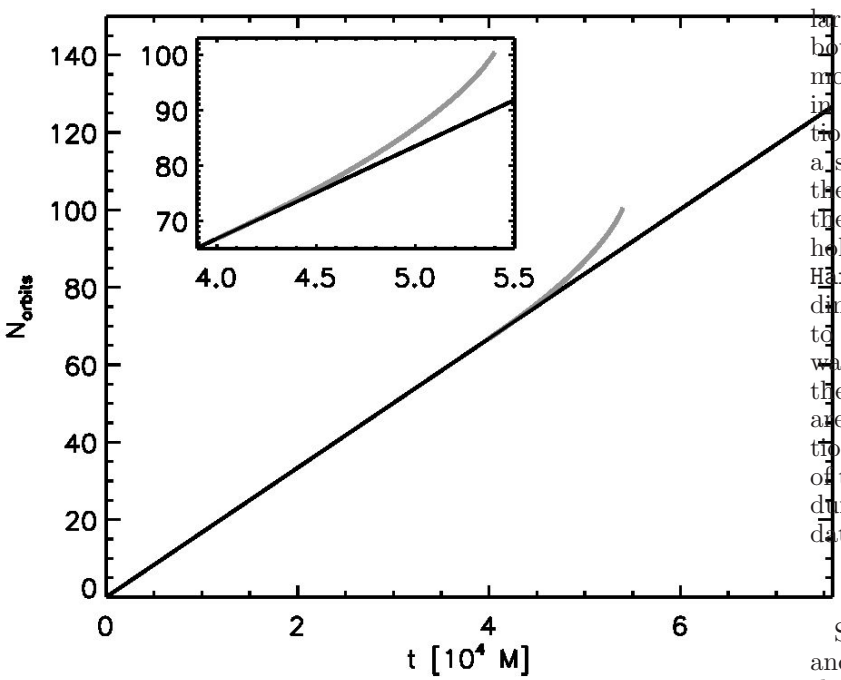

FIG. 3.— The number of orbits as a function of time. (Black) RunSS . (Grey) RunIn , in which the first part from $t = 0$ to $40000M$ shows the circular orbit without the radiation reaction.

as the binary is artificially kept at fixed a_0, while when $t > t_{\rm shrink}$, $N_{\rm orbits}$ can be approximated to leading order by

$$N_{\rm orbits} \sim \frac{1}{64\pi\nu}\left(\frac{a_0}{M}\right)^{5/2} = \frac{1}{64\pi}\left(\frac{a_0}{M}\right)^{5/2}\frac{(1+q)^2}{q}\,. \tag{10}$$

Therefore, for RunIn there are approximately 100 total orbits, while for RunSS there are approximately 127 orbits.

3. SIMULATION DETAILS

Like accretion disks around single black holes, circumbinary accretion flows are well described by the ideal MHD equations of motion (EOM) in the curved spacetime of only the black hole or holes. We therefore neglect the matter's contribution to spacetime curvature and the accumulation of mass and momentum by the black holes from gas accretion. Many codes have been written to simulate the single black hole case (e.g., Koide et al. (1999); De Villiers & Hawley (2003); Gammie et al. (2003); Noble et al. (2006); Anninos et al. (2005); Komissarov (2005); Tchekhovskoy et al. (2007); Noble et al. (2009)), while only the equations of electrodynamics (Palenzuela et al. 2009), force-free MHD (Palenzuela et al. 2010b,a) and nonmagnetized hydrodynamics (e.g., Bode et al. (2010); Farris et al. (2010, 2011); Bode et al. (2012)) have been solved in the relativistic circumbinary setting. Unfortunately, these latter simulations employ methods, like block-structured adaptive mesh refinement (AMR) in Cartesian coordinates, that typically lead to poor conservation of fluid angular momentum and excessive dissipation at refinement boundaries. These two effects alter the disk's angular momentum transport mechanism and thermodynamics in a nontrivial way. Furthermore, they require the solution of the Einstein equations, which—in turn—imposes a significant computational burden. In order to avoid these problems, we take an alternate route and solve the MHD EOM using a code designed for single black hole systems: `Harm3d` (Noble et al. 2009). Fortunately, `Harm3d` was written to be almost independent of coordinate system or choice of spacetime, so modifying it to handle non-axisymmetric, time-dependent spacetimes was straightforward. In fact, the only differences between the algorithm described in Noble et al. (2009) and here are that the metric (and its affine connection or gravitational source terms) needs to be updated every sub-step of the second-order Runge-Kutta time-integration procedure[5]. Below, we describe the equations solved, initial data setup and other details of the disk evolution.

3.1. *MHD Evolution*

Since we assume that the gas does not self-gravitate and alter the spacetime dynamics, we need only solve the GRMHD equations on a specified background spacetime, $g_{\mu\nu}(x^\lambda)$, where $\{x^\lambda\}$ represents a set of general spacetime coordinates. The EOM originate from the local conservation of baryon number density, the local conservation of energy, and the induction equations from Maxwell's equations (please see Noble et al. (2009) for more details). They take the form of a set of conserva-

[5] Note that many other technical changes were made that do not affect the algorithm, but do affect the runtime efficiency and design of the code.

tion laws:

$$\partial_t \mathbf{U}(\mathbf{P}) = -\partial_i \mathbf{F}^i(\mathbf{P}) + \mathbf{S}(\mathbf{P}) \tag{11}$$

where $\mathbf{U}$ is a vector of "conserved" variables, $\mathbf{F}^i$ are the fluxes, and $\mathbf{S}$ is a vector of source terms. Explicitly, these are

$$\mathbf{U}(\mathbf{P}) = \sqrt{-g}\left[\rho u^t,\, T^t{}_t + \rho u^t,\, T^t{}_j,\, B^k\right]^T \tag{12}$$

$$\mathbf{F}^i(\mathbf{P}) = \sqrt{-g}\left[\rho u^i,\, T^i{}_t + \rho u^i,\, T^i{}_j,\, \left(b^i u^k - b^k u^i\right)\right]^T \tag{13}$$

$$\mathbf{S}(\mathbf{P}) = \sqrt{-g}\left[0,\, T^\kappa{}_\lambda \Gamma^\lambda{}_{t\kappa} - \mathcal{F}_t,\, T^\kappa{}_\lambda \Gamma^\lambda{}_{j\kappa} - \mathcal{F}_j,\, 0\right]^T \tag{14}$$

where g is the determinant of the metric, $\Gamma^\lambda{}_{\mu\kappa}$ is the metric's affine connection, $B^i = {}^*F^{it}/\sqrt{4\pi}$ is our magnetic field (proportional to the field measured by observers traveling normal to the spacelike hypersurface), ${}^*F^{\mu\nu}$ is the Maxwell tensor, u^μ is the fluid's 4-velocity, $b^\mu = \frac{1}{u^t}\left(\delta^\mu{}_\nu + u^\mu u_\nu\right) B^\nu$ is the magnetic 4-vector or the magnetic field projected into the fluid's co-moving frame, and $W = u^t/\sqrt{-g^{tt}}$ is the fluid's Lorentz function. The MHD stress-energy tensor, $T_{\mu\nu}$, is defined as

$$T_{\mu\nu} = (\rho h + 2p_m)\, u_\mu u_\nu + (p + p_m)\, g_{\mu\nu} - b_\mu b_\nu \tag{15}$$

where $p_m = b^\mu b_\mu/2$ is the magnetic pressure, p is the gas pressure, ρ is the rest-mass density, $h = 1 + \epsilon + p/\rho$ is the specific enthalpy, and ϵ is the specific internal energy, We evolve the quantity $(\rho u^t + T^t{}_t)$ instead of $T^t{}_t$ in order to reduce the magnitude of the internal energy's numerical error (Gammie et al. 2003). Note that the terms proportional to $\Gamma^\lambda{}_{t\kappa}$ and $\Gamma^\lambda{}_{\phi\kappa}$ in the source no longer vanish as the metric is now dependent on time and azimuthal coordinate, ϕ. Also, note that we add a negative source term $(-\mathcal{F}_\mu)$ to the local energy conservation equation to model energy/momentum loss from radiative cooling; please see Section 3.4 for more details.

The MHD evolution is facilitated by calculating and using so-called primitive variables: the rest-mass density (ρ), the internal energy density ($u = \rho\epsilon$), the velocities relative to the observer moving normal to the spacelike hypersurface, $\tilde{u}^i = u^i - u^t g^{ti}/g^{tt}$. The magnetic field B^i is considered both a primitive and a conserved variable. We employ piecewise parabolic reconstruction of the primitive variables for calculating the local Lax-Friedrichs flux at each cell interface (Gammie et al. 2003). We use a 3-dimensional version of the FluxCT to impose the solenoidal constraint, $\partial_i \sqrt{-g} B^i = 0$ (Tóth 2000). The EMFs (electromotive forces) are calculated midway along each cell edge using piecewise parabolic interpolation of the fluxes from the induction equation. A second-order accurate Runge-Kutta method is used to integrate the EOM using the method of lines once the numerical fluxes are found. The primitive variables are found from the conserved variables using the "2D" scheme of Noble et al. (2006). A conservation equation for the entropy density is evolved and used to replace the total energy equation of the 2D method whenever the plasma becomes too magnetically dominated, or—specifically—when $\rho\epsilon < 0.02 p_m$; this procedure helps us avoid numerical instabilities and negative pressures from developing. Please see Noble et al. (2009) for more details.

The MHD evolution is performed in the same way as in single black hole cases except that the metric is evaluated[6] at the present sub-step's time before the MHD fields are updated. The metric is required in many facets of the update procedure. For example, it is used in calculating the 4-velocity from the primitive velocities, source terms and geometric factors in the EOM, and for deriving the primitive variables from the conserved variables. The affine connection is calculated via finite differencing the PN metric to evaluate

$$\Gamma^\mu{}_{\nu\kappa} = \frac{1}{2} g^{\mu\sigma}\left(\partial_\nu g_{\kappa\sigma} + \partial_\kappa g_{\nu\sigma} - \partial_\sigma g_{\nu\kappa}\right) \quad . \tag{16}$$

The spatial finite differences use fourth-order centered stencils away from the physical boundaries, and backward/forward stencils adjacent to the physical boundaries. Since the metric is evaluated and stored at the cell centers and faces, but the connection is only evaluated at the centers, fourth-order stencils require only three cells' worth of data to compute. The time derivatives are second-order accurate, but use a time spacing 10^{-3} times that used in the MHD integration. This means that additional evaluations of the metric are made at advanced and retarded times at the cell centers to calculate the time derivatives for each connection evaluation. We have verified that the truncation error from the time derivatives is smaller than that from the spatial derivatives. Also, the connection's spatial finite differencing is one order more accurate than that of the MHD procedure, implying it is not the primary source of error in the calculation. Please see Appendix B for a discussion on our resolution tests.

3.2. *Initial Conditions*

In this project, we avoid evolving the gas in the neighborhood of the black holes, choosing instead to focus on establishing reasonable prior conditions for the gas that ultimately feeds the BBH. We therefore excise a spherical domain, which includes the binary, from our calculation.

It is common to begin with initial conditions devoid of large transient artifacts. This is often done by starting from a torus of material in equilibrium (via pressure and rotational support) about the central gravitating source (e.g., a black hole) (Chakrabarti 1985; De Villiers et al. 2003). Unfortunately, such tori will not be near equilibrium in our spacetime as it is (t, ϕ)-dependent. Plus, the equations describing their structure assume that the metric has the same form (i.e. share the same zero-valued elements) as the Kerr metric in Boyer-Lindquist coordinates. We resolve these issues in the following way. First, since we hold the binary at fixed separation for several orbits, the spacetime initially has a helical Killing symmetry, with Killing vector $\mathcal{K}^a = \Omega_{\rm bin}\left(\partial_\phi\right)^a + \left(\partial_t\right)^a$. In other words, the spacetime is invariant in a frame rotating with the binary, while the separation is held constant. Since the torus will lie a few a_0 away from the binary, its dynamical response time—comparable to its orbital period—will be longer than the binary period, implying that a torus near equilibrium in this helically-symmetric spacetime will also be near equilibrium in its time average. Due to its helical symmetry, its time average is also

[6] We remind the reader that the metric is known in closed form, requiring only direct evaluation except for the Newton-Raphson iteration to find the current time's binary separation.

its azimuthal average. We therefore start with a torus in equilibrium in a (t, ϕ)-independent spacetime, $\hat{g}_{\mu\nu}$, found by averaging over ϕ:

$$\hat{g}_{\mu\nu} = \frac{\int g_{\mu\nu}\sqrt{g_{\phi\phi}}\, d\phi}{\int \sqrt{g_{\phi\phi}}\, d\phi} \quad . \tag{17}$$

We have verified that the same components that are zero-valued in Boyer-Lindquist coordinates are consistent with zero to within our PN-order accuracy in the $\hat{g}_{\mu\nu}$ metric. This means we can employ a similar torus solution method as described in Chakrabarti (1985). A description of our modifications to the procedure—including the generalization to our ϕ-averaged spacetime—is provided in Appendix A. Note that we now ensure that the equilibrium solution is found iteratively to greater precision, instead of the approximate method described in De Villiers et al. (2003) which has been used in prior work of the authors in single black hole disk evolutions (Noble et al. 2009, 2010) and by others studying the hydrodynamic circumbinary case (Farris et al. 2011). We find that our procedure produces initial tori that are much closer to equilibrium than the approximate scheme. Please see Appendix A for more details.

Previous studies have shown that a gap develops near $2.5a$ for equal mass binaries (MacFadyen & Milosavljević 2008; Shi et al. 2011). We aim to study how this gap develops, so we choose to start material outside this radius. We therefore set up a disk with inner edge located at $r_{\rm in} = 3a_0$ and pressure maximum located at $r_p = 5a_0$; from prior experience, r_p is approximately the radius at which the disk transitions from accreting to decreting since matter must shed its angular momentum to fluid elements further out in order to accrete. These outer elements gain angular momentum and form a time-averaged decretion flow away from the central potential. We will therefore focus on $r < r_p = 5a_0$ in our analyses. The initial disk extends to $r_{\rm out} \simeq 12a_0$, is isentropic with $p/\rho^\Gamma = 0.01$, and is tuned to have an aspect ratio of $H/r = 0.1$ at $r = r_p$, where H is the density scale height defined as the first moment of the rest-mass density with respect to distance from the midplane:

$$H \equiv \frac{\langle \rho\sqrt{g_{\theta\theta}}\, |\theta - \pi/2| \rangle}{\langle \rho \rangle} \quad , \tag{18}$$

and where the $\langle X \rangle$ denotes the average over origin-centered spheres:

$$\langle X \rangle \equiv \frac{\int X\, \sqrt{-g}\, d\theta d\phi}{\int \sqrt{-g}\, d\theta d\phi} \quad . \tag{19}$$

More information about the initial torus and its solution method is given in Appendix A. In the disk, we add random, cell-scale noise to the the internal energy, u, in order to hasten the development of turbulence; the random noise is evenly distributed over the range $\pm 5 \times 10^{-3}$.

Once the torus is in place on the grid, a surrounding nonmagnetized atmosphere is added as our numerical scheme requires us to maintain positive values of ρ and p. The atmosphere is initially static, $u^i = 0$, and in approximate pressure equilibrium: $\rho_{\rm atm} = 1 \times 10^{-7}\rho_{\rm max}\,(r/M)^{-3/2}$, $u_{\rm atm} = 3.3\times 10^{-6}\, u_{\rm max}\,(r/M)^{-5/2}$, where $\rho_{\rm max}$ and $u_{\rm max}$ are—respectively—the initial maxima of ρ and u. We note that when either ρ or u are found to go below, respectively, $\rho_{\rm atm}$ or $u_{\rm atm}$, they are set to those atmosphere values without any modification to the magnetic field or fluid velocity; this happens very rarely once the disk's turbulence saturates.

The magnetic field is initialized as a set of dipolar loops that follow density contours in the disk's interior. We set the azimuthal component of the vector potential and differentiate it to yield B^i; $B^\phi(t = 0) = 0$ in our configuration. The vector potential component is

$$A^\phi = A_0^\phi \max\left[\left(\rho - \frac{1}{4}\rho_{\rm max}\right), 0\right] \quad . \tag{20}$$

The magnitude of the field, A_0^ϕ, is set such that the ratio of the disk's total internal energy to its total magnetic energy is 100.

3.3. *Grid, Boundary Conditions, and Parameters*

The domain on which the MHD EOM are solved is a uniformly discretized space of spatial coordinates $\left\{x^{(i)}\right\}$ that are isomorphic to spherical coordinates $\{r, \theta, \phi\}$:

$$r(x^{(1)}) = M e^{x^{(1)}} \quad , \tag{21}$$

$$\theta(x^{(2)}) = \frac{\pi}{2}\left[1 + (1-\xi)\left(2x^{(2)} - 1\right) + \left(\xi - \frac{2\theta_c}{\pi}\right)\left(2x^{(2)} - 1\right)^n\right] \quad , \tag{22}$$

and $\phi = x^{(3)}$. We set $n = 9$, $\xi = 0.87$, and $\theta_c = 0.2$. The logarithmic radial coordinates are such that the radial cell extents are smaller at smaller radii in order to resolve smaller scale features of the accretion flow there. The $x^{(2)} \leftrightarrow \theta$ mapping concentrates more cells near the plane of the disk and the binary's orbit, the equator of our coordinate system. Let each grid cell in our numerical domain be labeled by three spatial indices that each cover $[0, N^{(n)} - 1]$, where $\left\{N^{(n)}\right\}$ are the number of cell divisions along each dimension. A cell with indices (i, j, k) is located at $\left(x_i^{(1)}, x_j^{(2)}, x_k^{(3)}\right)$, where $x_j^{(n)} = x_b^{(n)} + \left(j + \frac{1}{2}\right)\Delta x^{(n)}$. The grid we used is completely specified by: $x_b^{(1)} = \ln(r_{\rm min}/M)$, $\Delta x^{(1)} = \ln(r_{\rm max}/r_{\rm min})/N^{(1)}$, $r_{\rm min} = 15M$, $r_{\rm max} = 260M$, $N^{(1)} = 300$, $x_b^{(2)} = 0$, $\Delta x^{(2)} = 1/N^{(2)}$, $N^{(2)} = 160$, $x_b^{(3)} = 0$, $\Delta x^{(3)} = 2\pi/N^{(3)}$, $N^{(3)} = 400$.

We chose our resolution and grid extent based upon a number of criteria. First, our θ and ϕ resolutions were set in order to adequately resolve the MRI based on guidelines of Hawley et al. (2011) and Sorathia et al. (2011). The radial resolution was chosen to resolve the spiral density waves—generated by the binary's time-varying tidal field—by several radial zones. We find that our grid adequately resolves the MRI, as measured by the criteria of Hawley et al. (2011) and Sorathia et al. (2011), throughout the domain of interest (i.e. $r < 5a_0$) $\forall t$. Please see Appendix B for a quantitative description of these resolution criteria and for a demonstration of how well we resolve the MRI.

The radial extent of the grid was inspired by Shi et al. (2011) and the limits of our near-zone PN metric. Since the near-zone PN metric that we use is only valid at distances more than $10M_i$ from the black

hole with mass M_i (Yunes & Tichy 2006; Yunes et al. 2006; Johnson-McDaniel et al. 2009), then—in the equal mass case considered here—we have $r_{\rm min} \geq 10\frac{M}{2} + \max(a(t))/2 = 5M + a_0/2 = 15M$. Shi et al. (2011) found that an inner radial boundary located at $r_{\rm min} \lesssim 1.1a$ was sufficiently far away from the gap and deep in the potential as to not significantly alter the development and evolution of the surface density peak at the edge of the gap. These two constraints justify our choice of $r_{\rm min} = 15M = 0.75a_0$ and suggest that our inner boundary condition may begin affecting the gap's evolution when $a(t) \lesssim r_{\rm min}/1.1 \simeq 13.6M \simeq 0.68a_0$, which occurs after approximately $t = 51235M$ in RunIn . We set $r_{\rm max} = 260M = 13a_0$ to encompass the initial torus.

All cells are advanced in time with the same time increment ($\Delta x^0 = \Delta t$), which itself changes in time; Δx^0 is set to $0.45\Delta t_{\rm min}$, where $\Delta t_{\rm min}$ is the shortest cell crossing time of any MHD wave over the entire domain.

Boundary conditions were imposed through assignment of primitive variables and B^i in ghost zones. Outflow boundary conditions are imposed at $r = r_{\rm min}$ and $r = r_{\rm max}$ which amounts to extrapolating the primitive variables at $0^{\rm th}$-order into the ghost zones. Additionally, u^r is set to zero—and $\tilde{u}^i$ recalculated—whenever it points into the domain at $r = r_{\rm max}$. We note that we attempted to implement a similar condition on u^r at $r = r_{\rm min}$, but found it to be unstable during the earliest part of the simulation. Even though it was successfully used in MacFadyen & Milosavljević (2008) and Shi et al. (2011), we found that this condition was inconsistent with the tendency of negative radial pressure gradients developing ahead of each black hole as it moved around its orbit. This pressure gradient moves small amounts of material onto the grid, elevating the density just above the floor ahead of the black holes. Even without the special condition on u^r at $r_{\rm min}$ and just using $0^{\rm th}$-order extrapolation of the primitive variables there, we observe insignificant amounts ($\ll 1\%$ of the total) of positive mass flux into the domain there and a nearly flat $\dot{M}(r,t)$ profile over $r_{\rm min} < r < 2a$ with no noticeable artifacts near $r_{\rm min}$ (e.g., Figure 7).

3.4. *Thermodynamics*

Depending on internal properties of the gas (e.g., density, accretion rate), the disk may or may not be optically thin, geometrically thin, or have a constant aspect ratio H/r. As these disk characteristics are sensitive to the assumed initial conditions and thermodynamics of the system, we therefore must select which kind of disk to model *a priori* and verify the consistency of our assumptions *a posteriori*. We chose to model a disk with intermediate thickness ($H/r = 0.1$) in order to both address the fact that binary's torque will likely heat the gas efficiently and our expectation that the disk will be dense, optically thick and radiating efficiently.

We chose the ideal-gas "Γ-law" equation of state to close the MHD EOM: $P = (\Gamma - 1)\,\rho\epsilon$. We set $\Gamma = 5/3$, which reasonably well describes the behavior of a plasma whose specific thermal energy is smaller than an electron's rest-mass energy (i.e. it is not relativistically hot). The gas is cooled to a target entropy, the initial entropy of the disk, at a rate equal to

$$\mathcal{L}_c = \frac{\rho\epsilon}{T_{\rm cool}}\left(\frac{\Delta S}{S_0} + \left|\frac{\Delta S}{S_0}\right|\right) \quad , \tag{23}$$

where $\Delta S \equiv S - S_0$ and $T_{\rm cool} = 2\pi\,(r/M)^{3/2}$ is the cooling time, which we approximate as the Newtonian period of a circular equatorial orbit at radius r. Our procedure is similar to those used by Noble et al. (2009) and Penna et al. (2010). The term in the parentheses acts as a switch ensuring that $\mathcal{L}_c \geq 0$ always, and is zero when the local entropy, $S = p/\rho^\Gamma$, is below the target entropy, $S_0 = 0.01$, which is the constant value used in the initial data's torus. Hence, the cooling function should release any heat generated through dissipation since the initial state. We do not cool unbound material—i.e. fluid elements that satisfy $(\rho h + 2p_m)\,u_t < -\rho$—since we do not want to include cooling that results from application of density or pressure floors. Since $\mathcal{L}_c$ is the cooling rate in the local fluid frame, its implementation in the EOM must be expressed in the coordinate frame:

$$\mathcal{F}_\mu = \mathcal{L}_c u_\mu \quad . \tag{24}$$

Another advantage of the cooling function is that it provides us with a proxy for bolometric emissivity that is consistent with the disk's thermodynamics—unlike *a posteriori* estimates of synchrotron and/or bremsstrahlung luminosity that have typically been made in numerical relativity simulations (e.g., Bode et al. (2010); Farris et al. (2010, 2011)). We will use $\mathcal{L}_c$ to make predictions of the total luminosity from circumbinary disks. These predictions are made by integrating $\mathcal{L}_c$ over the domain in the coordinate frame; we expect to verify their accuracy using full GR ray-tracing in future work.

4. RESULTS

4.1. *Approximate Steady State*

At the beginning of both simulations, orbital shear transforms part of the radial component of the magnetic field to toroidal, creating a laminar Maxwell stress. Meanwhile, in the same region, the magnetorotational instability grows, its amplitude exponentially growing on the local dynamical timescale, $\simeq 500M$ at the initial inner edge of the disk, $r = 60M$. The turbulence in the inner disk reaches nonlinear saturation at $t \simeq 10000M$. Under the combined influence of the initial laminar and later turbulent Maxwell stress, matter flows inward (see Figure 4).

4.1.1. *Surface density*

Soon after $t \simeq 10000M$, the inward flow begins to pile up at $r \simeq 50M$, between two and three times the binary separation (the dashed line in both panels of Figure 4 marks the location of $2a(t)$ in order to guide the eye). We define the surface density Σ as

$$\Sigma(r,\phi) \equiv \int d\theta\sqrt{-g}\rho/\sqrt{g_{\phi\phi}(\theta = \pi/2)}; \tag{25}$$

when we quote it as $\Sigma(r)$, that denotes an azimuthal average of equation (25). In later discussion, we will sometimes normalize the surface density to Σ_0, the maximum surface density in the initial condition; in code-units $\Sigma_0 = 0.0956$. In RunSS , $\Sigma(r \sim 2a)$ grows steadily

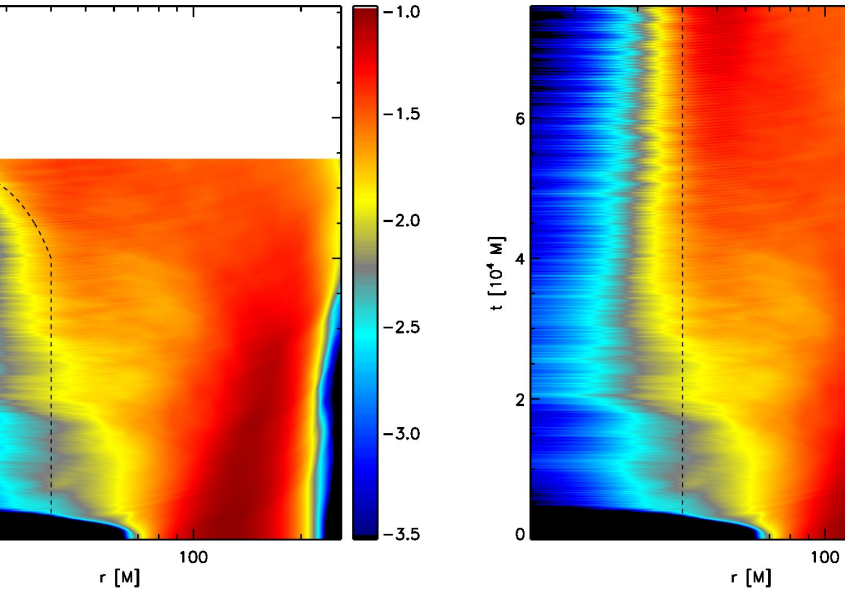

FIG. 4.— Color contours of $\log \Sigma(r)$ as a function of time. The scale is shown in the color bar. The black dashed curve shows $2a(t)$. (Left) RunIn . (Right) RunSS .

for the duration of the simulation, but after $t \simeq 20000M$, the logarithmic rate of growth (i.e. [illegible] ually becomes slower and slower. [illegible] of azimuthally-averaged properties [illegible] steadier after $t = 40000M$, we call t [illegible] until the end of RunSS the "quasi- [illegible] the same reason, we began the bina [illegible] of RunIn at that time.

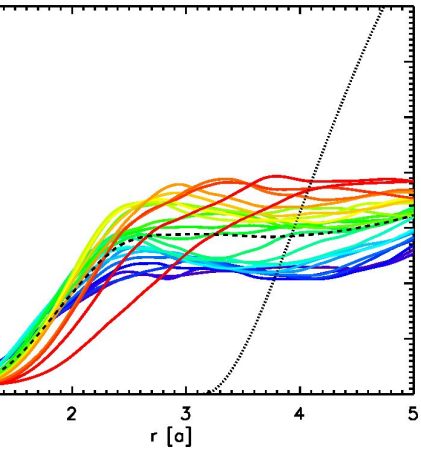

FIG. 5.— $\Sigma(r/a)$ every $1000M$ in time from $t = 30000M$ to the end of the simulation. Time increases from violet color to red. The dotted curve shows the initial condition. The dashed curve shows the average of the colored curves. (Left) RunIn , where the time span extends to $53000M$. Note that in this simulation a decreases after $t = 40000M$, so that a fixed value of r/a corresponds to a progressively smaller radial coordinate after that time. (Right) RunSS , where the time span extends to $76000M$. The binary separation is fixed throughout this simulation.

Once this quasi-steady state is reached, $\Sigma(r)$ rises sharply from the inner boundary at $r = 16M$ to $r \simeq 50M$, initially $\propto r^{2.5}$, but at late times in RunSS , $\propto \exp(3r/a)$ (Figure 5). At first, the azimuthally-averaged surface density profile forms a relatively flat plateau at radii greater than $50M \simeq 2.5a$, but by $t = 30000M$, a distinct local maximum appears at $r \simeq 50M$ and persists for the remainder of the simulation. This maximum is noticeably asymmetric in the sense that $|d\Sigma/dr|$ is always considerably smaller in the disk body (i.e., $r > 2.5a$) than in the gap-region inside $r = 2a$ (Figure 5). This behavior resembles closely what has previously been seen in the Newtonian regime (e.g., MacFadyen & Milosavljević (2008); Shi et al. (2011)).

By construction, the behavior of RunIn is identical to that of RunSS up to $t = 40000M$, when the binary inspiral was begun. In fact, at large radius, the behavior of the surface density profile in RunIn continues to be very similar to that of RunSS even after the binary begins to shrink. Near the surface density peak and at smaller radii, however, things change. In RunIn , the location of the peak moves inward as the binary becomes smaller, and the slope of the disk's inner edge becomes noticeably shallower as the inspiral accelerates. Comparing the curve of the dashed line in the RunIn panel of Figure 4 to the curving edge of the colors denoting higher surface density, one can see that the location of the disk's inner edge follows the evolution of the binary until shortly before the end of the simulation.

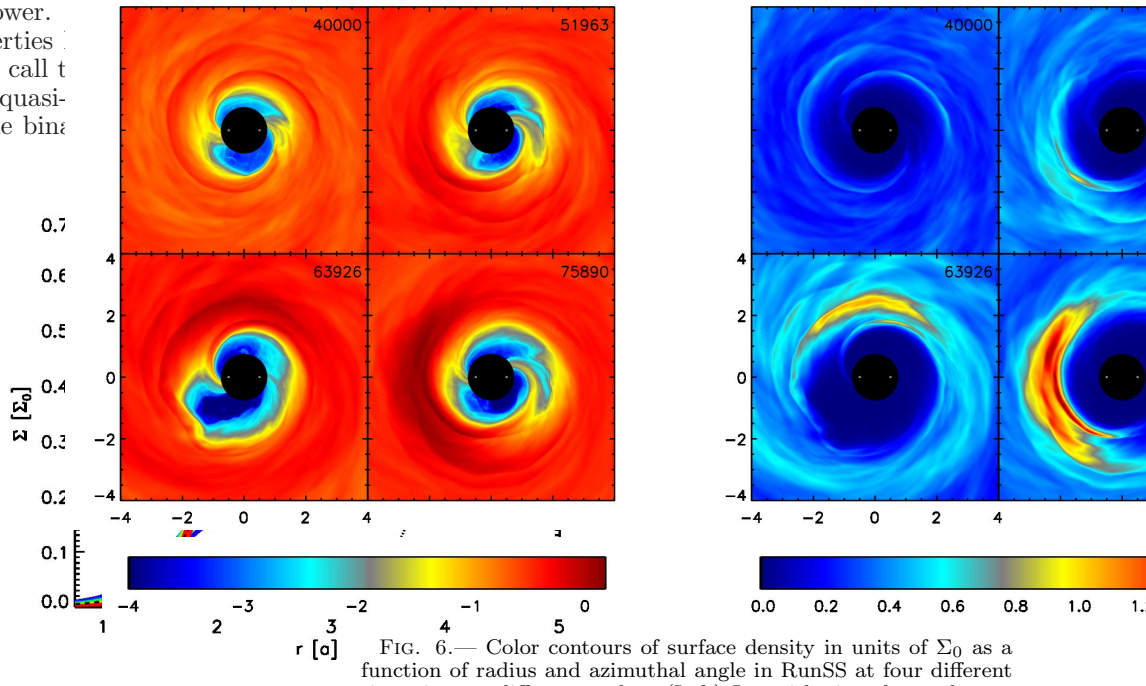

FIG. 6.— Color contours of surface density in units of Σ_0 as a function of radius and azimuthal angle in RunSS at four different times in two different scales: (Left) Logarithmic color scale emphasizing the streams from the disk toward the binary members. (Right) Linear color scale emphasizing the growth of asymmetry in the inner disk. In both panels, the times shown are $t = 40000M$ (upper-left), $t = 51963M$ (upper-right), $t = 63926M$ (lower-left), and $t = 75890M$ (lower-right).

However, speaking in terms of azimuthally-averaged surface density obscures an important aspect of circumbinary disks: near and inside their inner edges, their structure is generically far from axisymmetric. In Figure 6, we show $\Sigma(r, \phi)$ at $t = 40000M$. As mentioned previously, at radii smaller than $\simeq 2a \simeq 40M$, there is relatively little matter. The reason this gap forms is that,

unlike a time-steady, axisymmetric potential, the time-dependent quadrupolar potential of the binary does not conserve either the energy or the angular momentum of test-particles. Consequently, closed orbits do not exist, and torques driven by the binary can rapidly expel some matter to the outside, while matter on other trajectories can be forced inward (Shi et al. 2011). As a result, even though the rate at which matter enters the gap is comparable to the outer-disk accretion rate, at any given time, relatively little matter can be found in the region within $\simeq 2a$, and the matter that is present follows trajectories with little resemblance to stationary circular orbits. Instead, a pair of streams leave the inner edge of the disk and curve inward toward each member of the binary. Part of their flow gains enough angular momentum to return to the disk, but part crosses the inner simu boundary, traveling toward the domain of the bin

In addition, several tens of binary orbits afte ter begins to pile up at $r \simeq 2.5a$, a distinct " (as Shi et al. (2011) called it) forms in the reg the surface density peak. The density contrast be this lump and adjacent regions grows steadily in Thus, despite the relatively slow variation of azimu averaged disk properties during the period we call " steady", the "lump" continues to evolve secularl though RunSS was not continued long enough to s effect, Shi et al. (2011) found that the eccentricity lump's orbit also grows slowly.

4.1.2. *Accretion rate, internal stresses, and ang momentum budget*

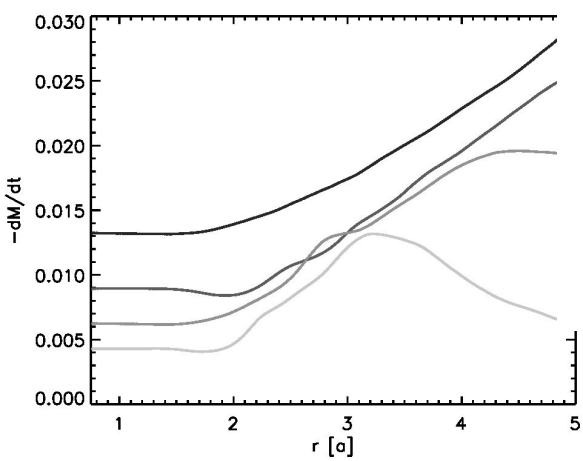

FIG. 7.— Time-averaged accretion rate during four equally spaced segments from $t = 30000M$ (black) till the end of RunSS . The curves becomes progressively lighter in shade as time advances.

It is also useful to characterize the global dynamics of circumbinary disks in terms of the radial dependence of the net mass flow, i.e., the accretion rate as a function of radius. We show in Figure 7 how this quantity slowly evolved during the quasi-steady epoch of RunSS by dividing the time from $30000M$ until the end of the simulation at $76000M$ into four segments and averaging over each one separately. The accretion rate is constant as a function of radius only inside the gap region, at most times increasing gradually outside $r \simeq 2a$. During the first part of this period, the accretion rate rises steadily to radii beyond $5a$, but after $t \simeq 50000M$, the accretion rate in the outer disk gradually falls. At the end of the simulation, $\dot{M}(r)$ is actually about a factor of 2 greater at $r \simeq 3a$ than anywhere else. Averaging over the entire quasi-steady epoch, the rate at which mass passes through the inner boundary is a bit less than half the accretion rate at $r = 5a$. Although the first analytic theories of circumbinary disks (Pringle 1991) assumed that *no* accretion would pass the inner edge of such a disk, Newtonian simulations, both purely hydrodynamic (MacFadyen & Milosavljević 2008) and MHD (Shi et al. 2011), have generally seen leakage fractions of a few tens of percent; our fraction is thus only somewhat greater than previously found.

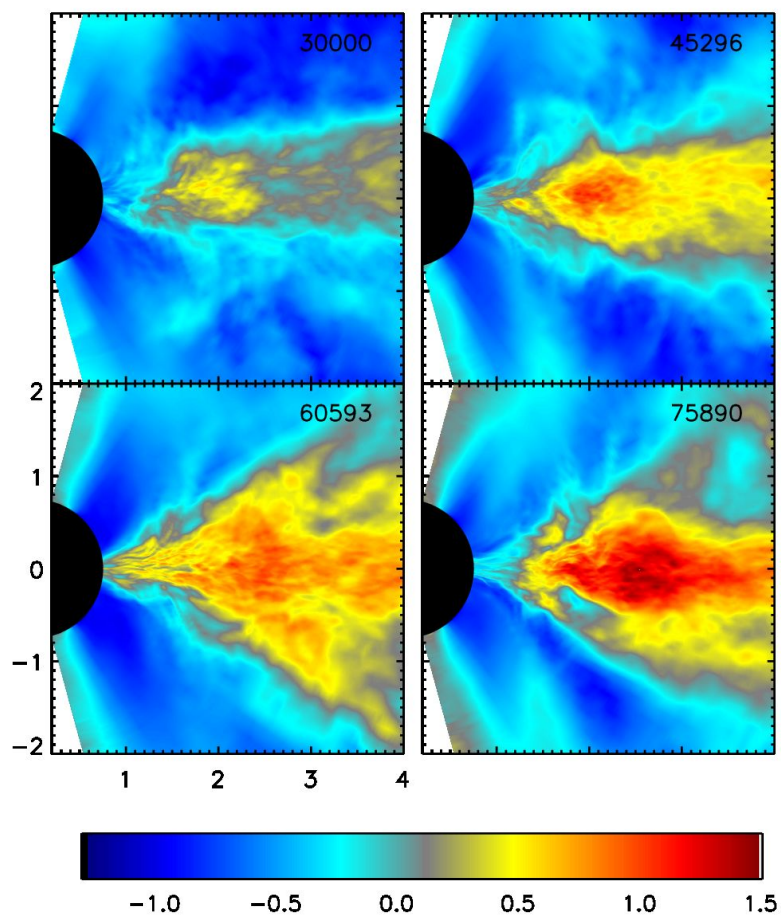

FIG. 8.— Log_{10} of the azimuthally-averaged plasma β parameter at four times during RunSS .

As mentioned earlier, Maxwell stresses due to correlations induced in MHD turbulence by orbital shear dominate angular momentum transport within accretion disks. Because the ratio of Maxwell stress to magnetic pressure, $2\langle B^{(r)}B_{(\phi)}\rangle/\langle B^2\rangle$, is fixed (Hawley et al. 2011) at $\simeq 0.3$–0.4 in a point-mass potential (here the notation $X^{(\mu)}$ denotes the magnitude of the μ-component of four-vector $\mathbf{X}$ projected into the fluid frame), the stress is linearly proportional to the magnetic pressure. A useful measure of the strength of magnetic effects is therefore the plasma $\beta \equiv \langle p\rangle/\langle B^2\rangle$. In most previous accretion disk simulations, this quantity is ~ 100 in the

midplane and drops to $\sim O(1)$ a few scale-heights the plane. We show its dependence on position poloidal plane at several times during the quasi-s epoch of RunSS in Figure 8; to be more precise, we the ratio of the time- and azimuthally-averaged gas sure to the similarly averaged magnetic pressure that figure illustrates, the level of magnetization is larger than usual (i.e., β is smaller than usual), but ually diminishes over time. At $t = 30000M$, $\beta \simeq 1$ midplane at $r \sim 3$–$5a$ and $\simeq 3$ in the region of the s density peak ($r \sim 2$–$3a$); by the end of the simulat is $\gtrsim 10$ in the disk body for the whole range $2a < r$ and reaches as much as $\simeq 30$ in the lump.

Ever since the work of Shakura & Sunyaev (19 has been popular to measure the vertically-integ azimuthally-averaged, and time-averaged interna stress in units of the similarly integrated and ave pressure. In order to avoid unphysical pressures in the unbound regions, we computed the stresse pressures only in bound material. Outside $r \sim 4a$, the disk resembles an ordinary accretion disk, w that the Maxwell stress alone has magnitude $\simeq 0$ in these units. This is roughly 3–5 times larger th stress levels found in general relativistic simulati MHD flows in the Kerr metric (Krolik et al. 200 the gap region, the ratio of Maxwell stress to pressure rises about a factor of 2, while the Reynolds stress in the gap rises dramatically (as also found by Shi et al. (2011)). These large Reynolds stresses are entirely due to the strong binary torque, which pushes part of the inflowing streams back out to the disk with additional angular momentum.

An overview of angular momentum flow in the system can be gleaned from Figure 9, in which we show the radial derivatives of the time-averaged angular momentum fluxes integrated on shells, i.e., the time-averaged torques due to the several mechanisms acting. Several important points stand out in this figure. The first is that the binary torques are delivered primarily in the gap region $a \lesssim r \lesssim 2a$. The torque density dT/dr peaks at $r \simeq 1.45a$, and the region surrounding that peak dominates the integral over all radii. Moreover, all these torques are positive in net, but they are locally negative both at small radii ($r \lesssim a$) and at large ($r \gtrsim 1.9a$). Thus, most of the angular momentum the binary gives the disk is delivered in the gap, where the gas density is very much lower than in the disk proper. This point has previously been emphasized by Shi et al. (2011). Second, that angular momentum is conveyed to the disk proper by fluid flows, i.e., Reynolds stresses. That is why the Reynolds stress is large and positive from $r \simeq 1.8a$ to $r \simeq 2.5a$. Outside those regions, Maxwell stress, which always acts so as to remove angular momentum from the gas and carry it outward, dominates the internal stresses. Finally, the net angular momentum change at any given radius is generally positive in the inner disk because matter continues to pile up between $r \simeq 2a$ and $r \simeq 5a$ throughout the simulation.

4.1.3. *Disk thickness*

We close this section by commenting on the disk thickness H/r [defined in Equation (18)], a parameter that will play an important role during the period when the

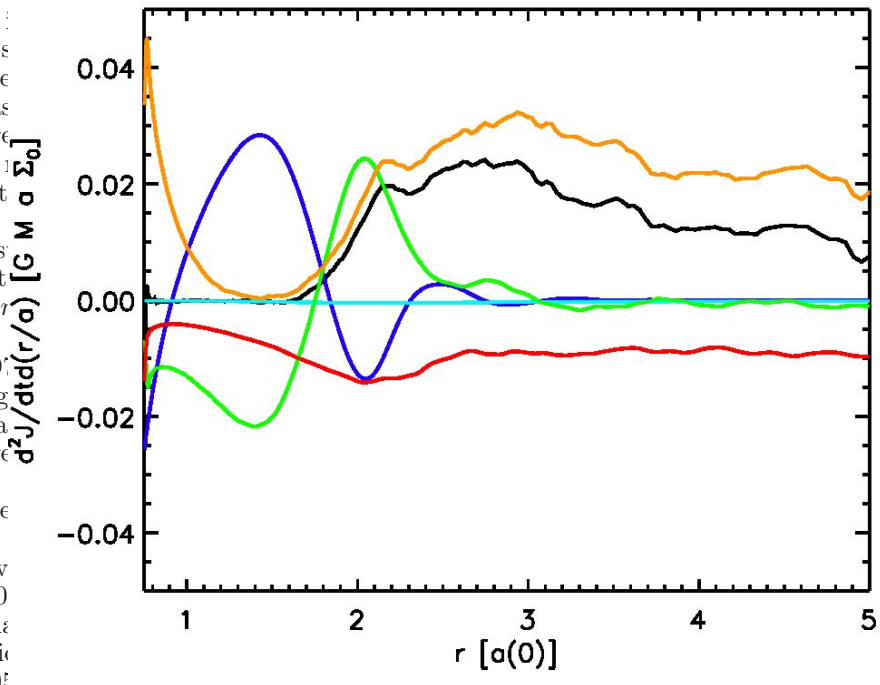

Fig. 9.— Radial derivatives of the angular momentum flux due to shell-integrated Maxwell stress in the coordinate frame (red), the angular momentum flux due to shell-integrated Reynolds stress in the coordinate frame (green), and advected angular momentum (gold). Torque densities per unit radius due to the actual binary potential and radiation losses are shown by blue and cyan curves, respectively. The net rate of change of angular momentum $\partial_r \partial_t J$ (solid black). All quantities are time-averaged over the quasi-steady epoch in RunSS .

binary orbit evolves. Our initial data and cooling function were chosen so as to keep H roughly constant over time at a fixed ratio to the local radius: $H/r \simeq 0.1$. However, although the gas temperature stayed very close to the target entropy at all radii $r > 2a$, and the ratio H/r did stay nearly independent of radius, its value first rose to $\simeq 0.15$ and then fell slightly (to $\simeq 0.12$ by the end of the simulation). The departure from the prediction of simple hydrostatic equilibrium was proportional to how much the magnetic pressure contributed to support against the vertical component of gravity.

4.2. *Binary Separation Evolution*

At $t = 40000M$ in RunIn , we began to evolve the binary orbit, letting it compress as gravitational radiation removes its orbital energy. The rate of orbital evolution is extremely sensitive to separation: $\dot{a}/a \propto a^{-4}$ when $a/r_g \gg 1$. Consequently, even at the relatively small initial separation assumed here ($a_0 = 20M$), orbital evolution is comparatively slow at first. However, it accelerates dramatically after $t \simeq 50000M$. By the end of RunIn ($t = 54000M$), $\dot{a}/a$ is quite rapid, and $a \simeq 8M$, small enough to make our PN expansion problematic.

While the binary orbit changes relatively slowly, the inner edge of the disk moves inward in pace with the change in the binary separation, staying close to $\simeq 2a(t)$ (as shown in Figures 4 and 10) until $t \simeq 50000M$. However, as the orbital evolution becomes more rapid (after $t \simeq 50000M$), although the inner edge of the disk continues to move inward in terms of absolute distance (Fig-

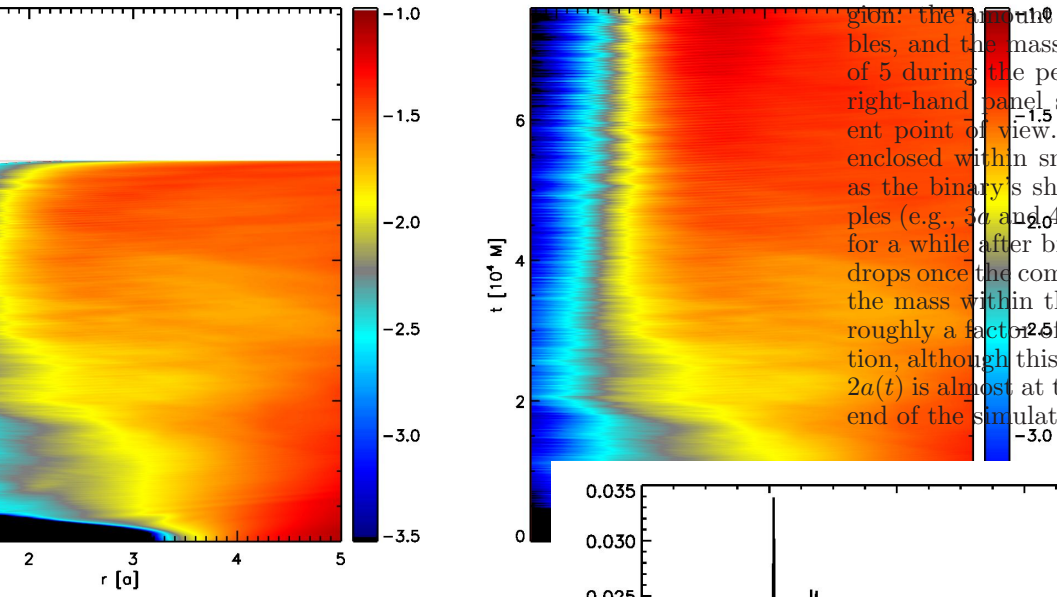

FIG. 10.— Color contours of $\log \Sigma(r/a($ in the color bar. (Left) RunIn . (Right) R

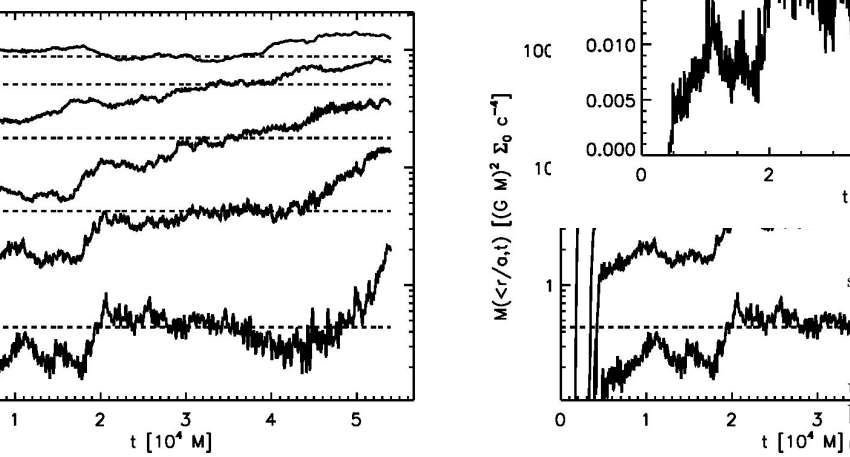

FIG. 11.— Mass enclosed within several sample radii as functions of time in RunIn . From bottom to top, the radii are $r/a = 1$, 1.5, 2, 3, and 4. (Left) For fixed $a = a_0$. (Right) For time-dependent $a(t)$.

ure 4), it begins to recede in terms of $r/a(t)$ (Figure 10). At the end of the simulation, the disk edge has moved in to $\simeq 20M$, but that is $\simeq 2.5a$. Simultaneous with this evolution, the slope of the inner edge also becomes gentler (Figure 5). In other words, the contrast between the surface density in the disk body and in the gap weakens, particularly when considering the outer part of the gap. As shown by the RunSS panel in Figure 10, none of this adjustment (in $r/a(t)$ terms) occurs without binary evolution.

Another view of this process may be seen in Figure 11. In that figure, we see the way matter accumulates in the inner disk over time, at first during the quasi-steady epoch and later during the binary orbital evolution of RunIn . The left-hand panel shows what happens when referred to an absolute radius scale. When the binary begins to shrink, the quantity of matter found at small radii grows abruptly, particularly in the original gap region: the amount of mass inside $r = 40M$ almost doubles, and the mass inside $r = 20M$ increases by a factor of 5 during the period of binary orbital evolution. The right-hand panel shows the same events from a different point of view. In this figure, we see that the mass enclosed within small multiples of $a(t)$ declines rapidly as the binary's shrinkage accelerates. For larger multiples (e.g., $3a$ and $4a$), the mass enclosed continues to rise for a while after binary orbital evolution, but eventually drops once the compression becomes rapid. In particular, the mass within the gap region (i.e., $r < 2a(t)$) falls by roughly a factor of 40 during the period of orbital evolution, although this ratio is in fact a bit ill-defined because $2a(t)$ is almost at the simulation's inner boundary by the end of the simulation.

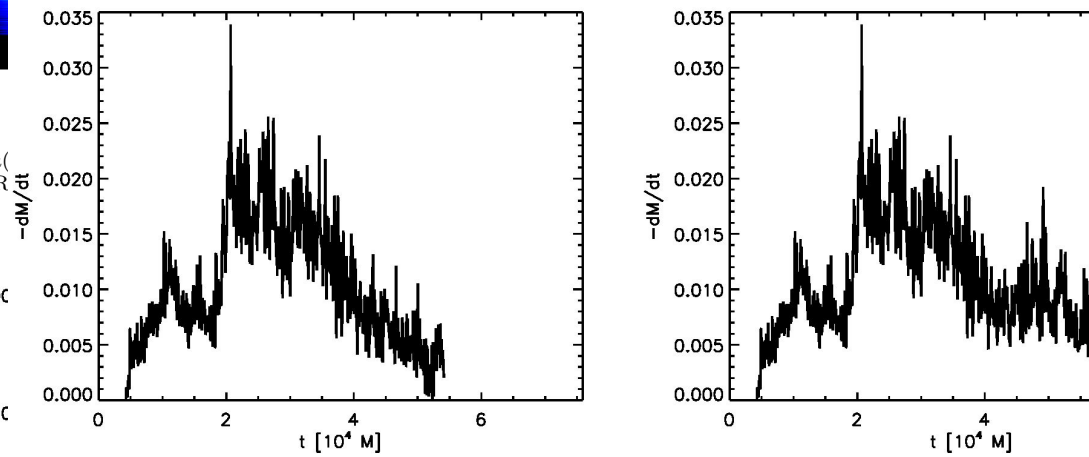

FIG. 12.— Accretion rate through the inner boundary of the simulation as a function of time. (Left) RunIn . (Right) RunSS .

The accretion rate behaves differently. It falls (see Figure 12) to $\simeq 30000M$–$40000M$, even before the binary begins to compress. Without binary orbital evolution (RunSS), it levels out from $\simeq 40000M$–$50000M$, before declining more gradually from $\simeq 50000M$ until the end of RunSS at $\simeq 76000M$. In RunIn , the onset of binary evolution at $t = 40000M$ leads to a continuing decrease in the rate at which mass flows through the inner boundary that levels out only after $\simeq 50000M$. Although the accretion rates in the simulations with and without binary orbital evolution decline at different times and at different rates, the final accretion rate in RunIn , when the binary separation has shrunk to $8M$, is only 20–30% less than at the same time in RunSS .

Another consequence of the changing relationship between disk material and the binary is a diminution in the integrated torque when the binary compresses (Figure 13). During the initial slow stages of energy loss due to gravitational wave emission, the binary continues to exert nearly as much torque on the disk as in RunSS , in which the binary orbit does not change at all. However, once the orbital shrinkage begins to accelerate, the torque plummets; at the end of RunIn , it has fallen to $\simeq 1/5$ of the value at that time in RunSS . The greater part of this diminution in torque is due to the fact that at this stage in the binary's evolution, its separation diminishes so rapidly that the region between a and $2a$, where most

of the torque is expressed, moves inward faster than the matter can follow. There is consequently much less matter on which these torques can be exerted. The connection between available matter and torque is shown clearly in the right-hand panel of Figure 13, in which one can easily see that for nearly the entire inspiral the torque density at the location of its maximum ($r = 1.45a(t)$) is almost exactly proportional to the surface density there. However, there is also a smaller part due to an artifact of the simulation. Its inner boundary lies at $r_{\rm min} = 15M$. As soon as $a(t)$ becomes smaller than $15M$, part of the region in which the binary torque is applied is no longer in the problem volume, so we cannot calculate any torque occurring there. As shown in the right-hand panel of Figure 13, this effect becomes significant at $t \simeq 5.2 \times 10^4 M$, when $a(t) \simeq 13M$. By the end of RunIn , $a \simeq 8M$, so that nearly the entire region where the torque is exerted ($a \lesssim r \lesssim 2a$) has left the problem volume. At that point, even if there were significant matter there, our calculation can neither say what its mass is nor what torque it feels.

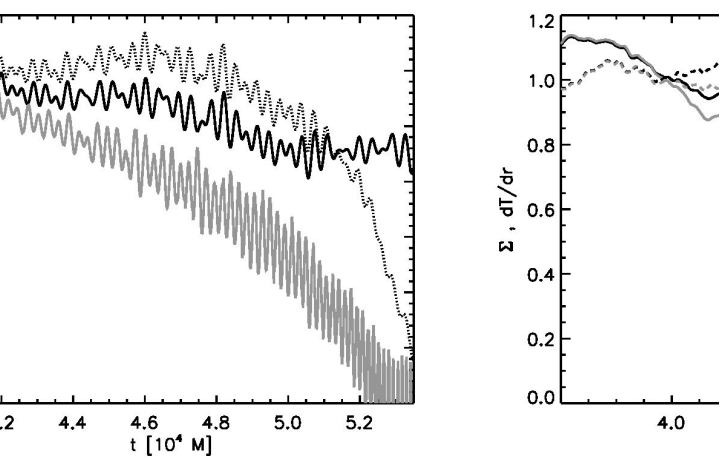

FIG. 13.— (Left) Integrated torque as a function of t RunSS (black) and RunIn (grey). Total torque is shown solid curves; the dotted curve shows torque in RunSS in only the radial range $r > r_{\rm min} a_0/a_2(t)$, where $a_2(t)$ is the separation as a function of time in RunIn . (Right) Surface (solid) and torque density at its peak, i.e., at $r = 1.45a(t)$ (d in RunSS (black) and RunIn (gray).

4.3. *EM Luminosity: Magnitude, Modulation*

We define the (coordinate frame) cooling rate per unit radius of the disk by

$$\frac{dL}{dr} = \int \sqrt{-g}\, d\theta\, d\phi \mathcal{L}_c u_t. \qquad (26)$$

During the approximate stationary state, it is best described in terms of two separate regimes. As shown in Figure 14, at large radius ($r \gtrsim 2a$), it is very well described by a power-law, $dL/d(r/a_0) \simeq 5 \times 10^{-4}(r/a_0)^{-2}\Sigma_0 a_0$. At around $r \simeq 2a$, the cooling rate per unit radius reaches a local maximum and declines inward. This distinction neatly corresponds to two different mechanisms for generating the requisite heat: the dissipation of MHD turbulence associated with mass accretion (at large radius) and the dissipation of fluid kinetic energy given to the relatively small amount of gas in the gap by the binary torques (at small radius). In fact, this identification is confirmed semi-quantitatively. In time-steady accretion, the luminosity per unit radius is $(3/2)\dot{M}c^4/[(r/r_g)^2 GM]$ at radii where the local orbital angular momentum per unit mass is large compared to the net angular momentum flux per unit mass. Our disk is never in inflow equilibrium, and this expression is not exact when $\dot{M}$ is a function of radius. Nonetheless, taking it as an estimator, it predicts

$$\frac{dL}{dr/a_0} = 4 \times 10^{-4}(\dot{M}/0.01)(r/a_0)^{-2}\Sigma_0 a_0. \qquad (27)$$

As Figure 7 shows, the mean accretion rate in code units at $r = 2a$ in RunSS was $\simeq 0.01$, while $\dot{M}$ at larger radii is typically similar or perhaps a factor of two greater. Thus, this prediction of the luminosity profile on the basis of the time-averaged accretion rate and expectations derived from time-steady accretion onto a solitary mass quite accurately matches the actual luminosity profile seen in the simulation.

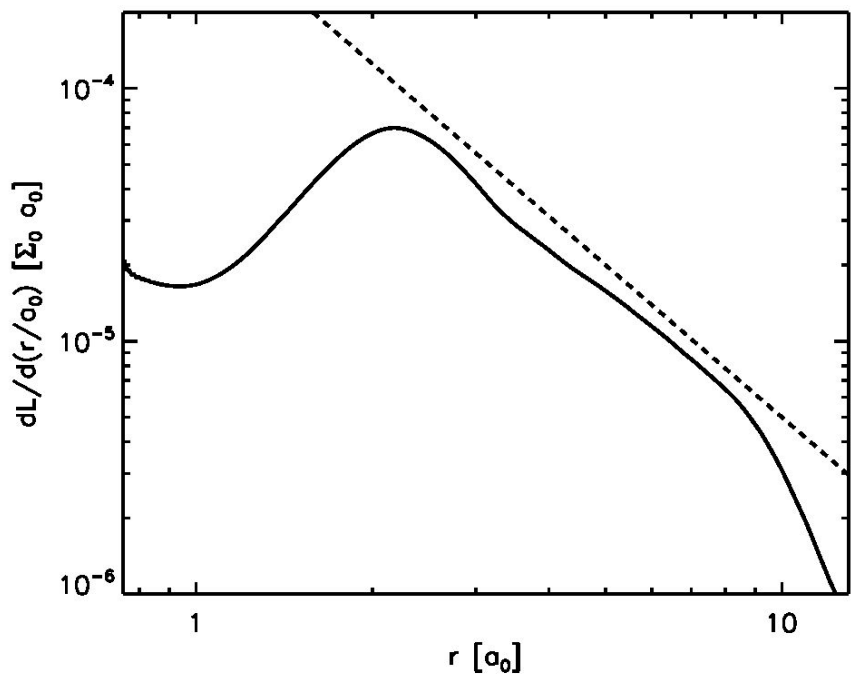

FIG. 14.— Luminosity per unit radius averaged over the quasi-steady epoch in RunSS . The dashed line shows a logarithmic slope of -2.

Integrated over radius, the total luminosity reaches a peak $\hat{L} \simeq 5.5 \times 10^{-3}$ at $t \simeq 33000M$ (Figure 15), where $\hat{L}$ is the integrated luminosity in units of $GM\Sigma_0 c$. After reaching this peak, $\hat{L}$ falls slowly, reaching $\simeq 3 \times 10^{-3}$ at $t \simeq 76000M$ in RunSS ; averaged over the entire quasi-steady period in this simulation, it is 3.8×10^{-3}.

The light output from RunIn remains very close to that in RunSS until the binary orbital evolution becomes rapid at $t \simeq 50000M$. After that time, it falls more sharply, so that by the time at which RunIn stops, $\hat{L} \simeq 2.7 \times 10^{-3}$; this is, however, still 2/3 the luminosity in RunSS at the same time. As the binary shrinks, the radial distribution of the luminosity changes in parallel,

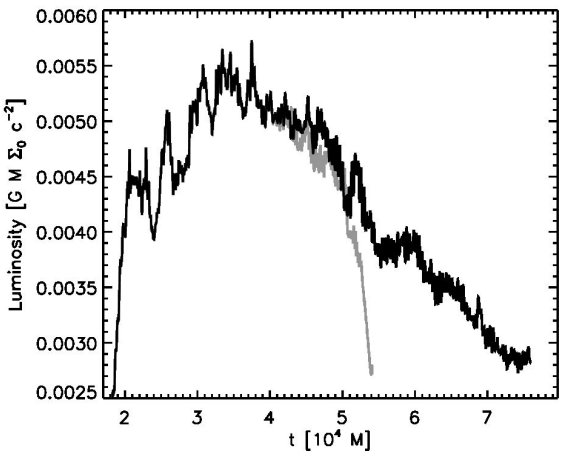

FIG. 15.— Luminosity as a function of time. (Grey) RunIn . (Black) RunSS . We note that the vertical axis' range does not include zero in order to accentuate the curves' fluctuations.

with the peak in surface brightness moving inward. We attribute the gradual decline in luminosity to the gradual decline in accretion rate. The sharp drop in the final stages of binary orbital shrinkage is due to the interaction of a boundary effect with genuine dynamics. As shown by Shi et al. (2011), gas streams flow inward from the inner edge of a quasi-steady circumbinary disk to radii $\simeq 1.2a$, where they can be strongly torqued and some of their material flung back outward toward the disk. The outward-moving matter shocks against the disk proper at a radius near that of the surface density peak, and the heat dissipated in these shocks contributes significantly to the luminosity. When the binary shrinks, this mechanism is weakened for two reasons. The inner boundary of our simulation ($r = 0.8a_0$) eventually becomes larger than $1.2a(t)$; when it does, matter is no longer thrown outward by binary torques. At the same time, however, it is possible that the retreat of the disk's inner edge when measured in terms of $a(t)$ might also lead to weaker inward streams.

The fact that the energy deposited by binary torques is ultimately radiated in the disk proper leads to a method of estimating the relative contributions to the total luminosity coming from accretion and binary torques. For that reason, and also because the accretion rate diminishes as the region of the surface density peak is approached from larger radius, it is a reasonable approximation to suppose that most of the luminosity from the region of the surface density peak inward has its source in the binary torques. We can therefore estimate the work done by the torques by bounding it between $L(r < 2a_0)$ and $L(r < 3a_0)$. On this basis, accretion would account for $\simeq 1/2$–$3/4$ of the total (i.e., $\hat{L} \simeq 1.8$–2.9×10^{-3}) and the binary torque for $\simeq 1/4$–$1/2$ ($\hat{L} \simeq 0.9$–2×10^{-3}).

The rest-mass efficiency of this luminosity is comparable to the rest-mass efficiency due to accretion that goes all the way to the black hole. Measured in terms of the time-dependent luminosity relative to the time-averaged accretion rate through the inner boundary, the efficiency in RunSS falls from a peak $\simeq 0.06$ achieved for $20000M \lesssim t \lesssim 45000M$ to $\simeq 0.03$ at the end of this simulation. There are several reasons that this efficiency is so great even though the potential at $r = 50M$ is an order of magnitude shallower than the potential at the innermost stable circular orbit (the "ISCO"). One is that the accretion rate in the circumbinary disk is roughly twice the accretion rate through the inner boundary, so the local accretion dissipation in the disk is boosted by that same factor of two relative to the rate at which mass passes the inner boundary. Another is that in a conventional disk around a single black hole the dissipation rate in the region just outside the ISCO is depressed relative to larger radii because some of the potential energy released is transported outward by the inter-ring stresses. In the Novikov-Thorne model (in which the stresses are assumed to vanish at the ISCO), almost 40% of the total luminosity is released outside $r = 40M$ when the black hole has no spin. This fraction is smaller when the spin is greater, and may be further reduced to the degree that the net angular momentum flux is smaller (Krolik et al. 2005). Lastly, of course, additional energy is deposited in the disk by the work done by the binary torques.

Translating the peak cooling rate into physical units gives

$$L_{\rm disk} \simeq 2.4 \times 10^{40} (\hat{L}/10^{-3}) M_6 \tau_0 \text{ erg/s}. \qquad (28)$$

Here τ_0 is the Thomson optical depth through a disk of surface density Σ_0 and $\hat{L}$ is the luminosity in code units, i.e., 3–5×10^{-3}. In Eddington units, this becomes $L_{\rm disk}/L_E \simeq 1.7 \times 10^{-4} (\hat{L}/10^{-3}) \tau_0$. Thus, for such a system to be readily observable at cosmological distances, it will be necessary both for the disk to be optically thick to Thomson scattering and for the mass of the binary to be relatively large. As a gauge of what might reasonably be expected, we note that in a steady-state accretion disk around a solitary black hole, the optical depth of the disk at $r/r_g = 20$ would be $\sim 2 \times 10^3 (\alpha/0.1)^{-1} (\eta/\dot{m})$, where η is the usual rest-mass efficiency and $\dot{m}$ is the accretion rate in Eddington units. With this disk surface density, the luminosity would approach that of a typical AGN when M_6 is at least ~ 1.

If this light were radiated thermally, the corresponding effective temperature would be

$$T_{\rm eff} \simeq 4 \times 10^4 (\hat{L}/10^{-3})^{1/4} M_6^{-1/4} \tau_0^{1/4} \text{ K}, \qquad (29)$$

where we have assumed that the radiating area is $2\pi(2a)^2$. Thus, it would emerge primarily in the ultraviolet for fiducial values of black hole mass and optical depth.

The luminosity (assumed to be optically thin) exhibits a noticeable modulation as a function of time, with peak-to-trough contrast of $\simeq 5\%$. Its Fourier power spectrum shows a strong, sharp peak at a frequency $1.47\Omega_{\rm bin}$ (see Figure 16) and a weaker peak at $0.26\Omega_{\rm bin}$. The latter is the orbital frequency at the radius of the surface density maximum, $\simeq 2.4a$; because the lump is located at this radius, we call this frequency $\Omega_{\rm lump}$. The former we identify with the rate at which the lump approaches the orbital phase of a member of the binary, $2(\Omega_{\rm bin} - \Omega_{\rm lump}) = 1.46\Omega_{\rm bin}$. When the lump draws near one of the black holes, a new stream forms, falls inward, and is split into two pieces, one of which gains angular momentum, sweeps back out to the disk, and ultimately shocks against the disk gas. It is this process, whose frequency is $1.46\Omega_{\rm bin}$, that modulates the light curve. If the binary mass ratio were far from unity, we expect that the modulation frequency would fall to $\simeq \Omega_{\rm bin} - \Omega_{\rm lump}$.

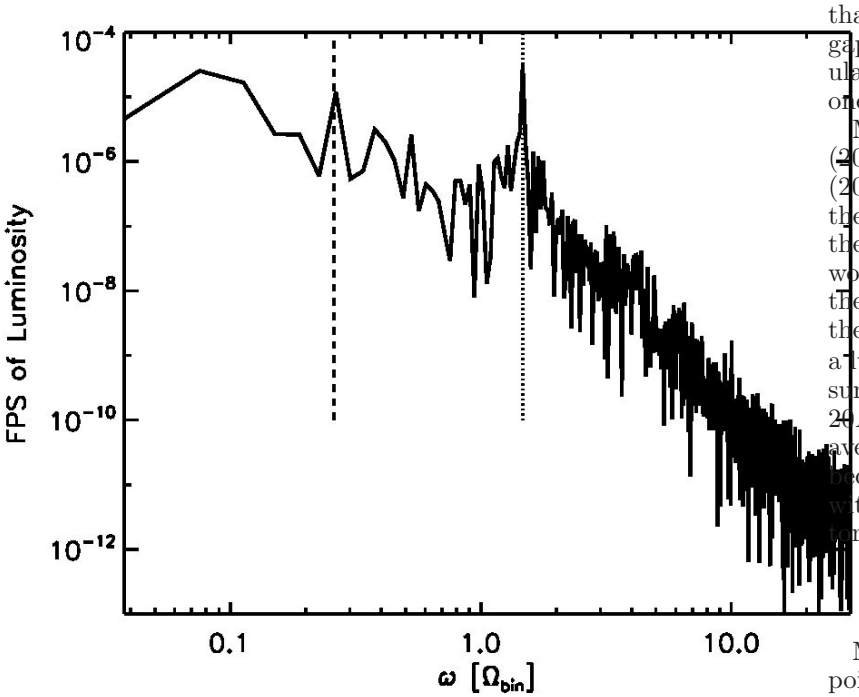

FIG. 16.— Fourier power spectrum of the luminosity radiated during the quasi-steady epoch of RunSS . The vertical lines represent: the orbital frequency at the surface density maximum (dashes) and the peak in the spectrum (dots).

5. DISCUSSION

5.1. *Comparison to Newtonian MHD*

In many respects, the behavior we found in this post-Newtonian regime resembles what was previously found in the Newtonian limit (Shi et al. 2011). There is very good agreement in the shapes of their azimuthally-averaged surface density profiles, with any contrasts attributable to their somewhat different initial conditions. In both cases, during the quasi-steady epoch the surface density at the disk's inner edge rises $\propto \exp(3r/a)$, reaches a maximum at $r \simeq 2.5a$, and then declines to larger radii.

At early times in both, there is a pair of streams leading from the disk edge to the inner boundary, which they typically reach at an orbital phase slightly ahead of the nearest member of the binary. Both also develop a strong $m = 1$ asymmetry (a "lump") in the surface density at $r \simeq 2.5a$ at late times. This asymmetry ultimately causes, in both the Newtonian and post-Newtonian simulations, a single stream in the gap to become dominant. Almost the only contrast in this regard is that the orbit of the lump developed a growing eccentricity in the Newtonian case, but not in RunSS .

The level of magnetization is likewise qualitatively similar: the mean plasma β in the Newtonian case fell from ~ 1 at $\simeq 6a$ to $\simeq 0.3$ at $r \simeq 2a$, while the value (averaged over the quasi-steady epoch in RunSS) in our simulations was $\simeq 1.5$ at $r = 6a$, grew to $\simeq 2.5$ at the surface density peak, and then decreased inward. The magnetic stress-to-pressure ratio α in the disk body follows the same pattern of close resemblance. It was $\simeq 0.3$ in the disk body in the Newtonian case, and $\simeq 0.2$ in RunSS . In the gap, the similarity was more qualitative than quantitative: in both cases, it rose steeply into the gap, but reached only $\simeq 0.7$ at $r \simeq a$ in the PN simulation, whereas it climbed to $\simeq 10$ in the Newtonian one.

Most strikingly, the luminosity estimated by Shi et al. (2011) scales extremely well to the PN case. Shi et al. (2011) could not directly compute the luminosity because they assumed an isothermal equation of state. However, they argued that the work done by the binary torques would be delivered to the disk and ultimately dissipated there into heat. Rewriting in our units their value for the rate at which the torques did work on the gas gives a luminosity of $0.018GM\Sigma_p c(a/r_g)^{-1/2}$, where Σ_p is the surface density at the maximum; for our separation ($a = 20M$) and our surface density at the maximum ($\simeq 0.55$ averaged over the quasi-steady epoch in RunSS), that becomes $2.2 \times 10^{-3} GM\Sigma_0 c$. This prediction agrees well with the upper end of our estimated range for the binary torque share of the luminosity.

5.2. *Comparison to Analytic Estimates of Binary Runaway*

Milosavljević & Phinney (2005) predicted that at some point well before the merger, the BBH should begin compressing so fast by gravitational radiation that internal stresses within the disk would not allow it to move inward rapidly enough to stay near the binary. At the order of magnitude level, this breakaway point would be expected to come when the gravitational radiation time

$$t_{\rm gr} = \frac{5}{64}\left(\frac{a}{M}\right)^4 \frac{(1+q)^2}{q} M \tag{30}$$

becomes shorter than the characteristic disk inflow time

$$t_{\rm in} = \alpha^{-1}(H/r)^{-2}(d\ln\Sigma/d\ln r)^{-1}\Omega^{-1} = \alpha^{-1}(H/r)^{-2}(d\ln\Sigma/d\ln r)^{-} \tag{31}$$

In these equations Ω is the local disk orbital frequency. The logarithmic derivative of the surface density enters because spreading of the inner edge is more rapid when it is especially sharp.

With a typical estimate of the stress level, $\alpha \sim 0.01$, the binary separation at which $t_{\rm gr}$ and $t_{\rm in}$ would match, and the disk and binary might decouple is

$$a_{\rm dec} = 70(d\ln\Sigma/d\ln r)^{-2/5}\left(\frac{H/r}{0.15}\right)^{-4/5} M, \tag{32}$$

where the fiducial radius at which the inflow time was computed is $r_* = 2a$, and we set $q = 1$. Indeed, it was this sort of estimate that led us to choose the initial conditions for our simulation.

However, scaling to the actual parameters of our simulation leads to a considerably smaller predicted value,

$$a_{\rm dec} \simeq 10[(d\ln\Sigma/d\ln r)/6]^{-2/5}\left(\frac{\alpha}{0.2}\right)^{-2/5}\left(\frac{H/r}{0.15}\right)^{-4/5} M, \tag{33}$$

which is much closer to what is found in RunIn . Thus, the substantially stronger magnetic stresses than predicted by usual α-based estimates lead to decoupling at a much smaller binary separation. Nonetheless, in the end the inward motion of the disk is limited by angular momentum transport, so once the magnitude of those stresses are known, $a_{\rm dec}$ can be estimated quite well by this means.

On the other hand, the meaning of the term "binary runaway" should also be made more nuanced. As we have seen, the accretion rate through the simulation inner boundary decreases as the binary shrinks, but almost the same decrease in accretion rate occurs when the binary *does not* shrink. Moreover, the continuing advance of the disk during the period of orbital evolution brought matter rapidly inward. The amount of matter within $30M$ rose by about a factor of 4 while the binary shrank, so that almost as much matter could be found within that radius as had been within $40M$ at the beginning of the binary orbital evolution. Thus, acceleration of binary orbital evolution does lead to a state in which the surface density at $r < 3a$ is smaller than would be expected if the orbital evolution were slower, and this diminution in the mass close to the binary does lead to consequences such as sharply diminished torque (as discussed in Section 4.2) and luminosity (see Section 4.3). On the other hand, neither the torque nor the luminosity falls by as much as an order of magnitude because the decoupling of binary and disk matter is not complete. Most notably, accretion continues at a rate only tens of percent lower than in the absence of inspiral.

Continuing accretion into the binary orbital region has a particularly interesting consequence. The material in those streams should, just as happens when the binary orbital evolution is slower, be captured into orbit around one or the other of the members of the binary. It will then settle into two smaller disks, one around each black hole. In the conditions of our simulation, the inflow time in the individual black hole disks might be only slightly shorter than the merger time because decoupling occurs when the binary separation is not a great deal larger than the ISCO, even if both black holes spin rapidly. If the circumbinary disk were cooler than in our simulation, so that $a_{\rm dec} \gg M$, the inflow time in the smaller disks would be shorter than that in the circumbinary disk by a sizable ratio: $\sim 3\times10^{-4}$ at decoupling if the scale heights in the inner disks and the outer disk are the same, and even smaller at later times. In either case, there could be interesting hydrodynamic interaction between the two smaller disks as the binary compresses.

5.3. *Different Disk Thermal States*

In terms of an ultimate comparison to observations, a larger question is posed by the disk's thermal state. As just shown, the binary separation at decoupling scales as $(H/r)^{-4/5}$, so the disk's internal pressure ($H \propto c_s \propto (p/\rho)^{1/2}$) can influence $a_{\rm dec}$. For reasons of numerical convenience, we chose parameters yielding a relatively thick disk. Although the factors controlling the saturation of magneto-rotational turbulence are still not well understood, a scaling with disk pressure remains plausible. If the effective sound speed of the gas were lower, decoupling might occur at rather larger binary separation, well outside the domain of relativistic orbits.

Several factors can influence the actual equation of state of the disk. In ordinary AGN, local heating due to accretion can make the disk radiation-dominated inside $r \simeq 100M$ when $\dot{m} \gtrsim 0.3$ and the central mass $M > 10^6 M_\odot$ (Krolik 1999). Larger central masses lead to radiation dominance even when $\dot{m}$ is smaller. When the disk surrounds a binary, the local heating should be similar at radii $r \gtrsim 2a$, as shown by Figure 14; the diminished accretion inside $\sim 4a$ is compensated by dissipation of the work done by the binary torques and delivered to the disk. In those circumstances, the disk scale height for $r \gtrsim 2a$ is independent of radius, giving an aspect ratio $H/r \simeq (3/2)(\dot{m}/\eta)(r/r_g)^{-1}$, where $\dot{m}$ is now the *local* accretion rate in Eddington units. Thus, our aspect ratio of $\simeq 0.15$ would correspond to a nominal $\dot{m} \simeq 0.4(r/40r_g)$; that is, this $\dot{m}(r)$ is the mass accretion rate at r that would, if it reached the black hole in a flow with $\eta = 0.1$, produce that fraction of an Eddington luminosity.

Given the relatively large leakage fraction through the inner edge of the circumbinary disk, the accretion rate onto the two black holes will in general be smaller than the accretion rate in the disk by only a factor of a few. They might therefore generate a sizable luminosity with a spectrum not too different from that of a generic AGN. Because the density in the gap is considerably smaller than in the disk, this luminosity may irradiate the disk, particularly if it is relatively thick. The inner edge of the disk could be heated by this means, as well.

Thus, there remains considerable uncertainty in the thickness profile of a circumbinary disk surrounding a relatively compact binary black hole. The particular thickness we have simulated lies within that range of uncertainty, but may not be generic.

5.4. *Distinctive EM Signals*

Given a sufficient external mass supply rate, the luminosity from the circumbinary disk alone could be great enough to be detected, even from a cosmological distance (Section 4.3). However, until the binary separation becomes as small as that considered here, the luminosity from matter accreting onto the two individual black holes would dominate the circumbinary luminosity by a large ratio. In many respects, a binary black hole with $a \gg 10M$ should strongly resemble a conventional AGN. However, when the separation is as small as the $\sim 20M$ scale studied in our simulations, contrasts with ordinary AGN continua might occur due both to the additional heating near the inner disk and the gap from $\sim 2.5a$ down to $\sim a/3$ in the range of radii in which a thermal disk exists. The supplementary heating due to the binary torques will increase the luminosity of the portion of the disk near $r \simeq 2a$, but the temperature in this region is smaller than the hottest part of the accretion flow by a ratio $\sim (1.5r_{\rm ISCO}/2a)^{3/4}$, where the factor 1.5 multiplying the ISCO radius is meant to account approximately for the displacement of the temperature maximum from the ISCO. Consequently, the additional luminosity will appear at rather longer wavelengths than the peak of the thermal continuum. On the other hand, radiation from the gap region will be very different from what might be expected from a conventional disk in those radii. The dissipation rate is much smaller because the motions are laminar, not turbulent; moreover, whatever light does issue from that region is unlikely to be effectively thermalized, and would therefore emerge at considerably shorter wavelengths. Thus, the luminosity at wavelengths intermediate between those characteristic of the innermost part of the disk and those characteristic of $r \simeq 2a$ would be significantly suppressed.

The periodic modulation in the heating rate of the

circumbinary disk that we have found might make its emission easier to isolate. The key question governing that "might" is how effectively optical depth in the disk blurs the modulation. Our cooling function, which operates at a characteristic rate $\sim \Omega(r)$ filters out variations on timescales $\ll \Omega^{-1}$, but optical depth would impose a rather more severe upper bound on the maximum effective frequency of variation. According to Kylafis & Klimis (1987), a constant-density sphere of radius R and optical depth τ suppresses the amplitude of a periodic signal of angular frequency ω injected at its center by a factor $\simeq 3c/(R\tau\omega)$ when $\omega R\tau/c \gg 1$. To apply this estimator, we suppose that a stratified disk segment with scale height H can be approximated by a homogeneous sphere of radius $R = H$. For binary separation a, the relevant orbital radius is $\simeq 2.5a$ and the signal frequency $\omega = 1.46\Omega_{\rm bin} \simeq 1.5(GM/a^3)^{1/2}$ for total binary mass M. As shown in Figure 6, the surface density in the lump grows to be $\simeq \Sigma_0$, so we take $\tau = \tau_0$. The suppression factor is then $\simeq 0.024(\tau_0/1000)^{-1}(a/20r_g)^{1/2}(H/0.15r)^{-1}$. In other words, when the relevant region of the disk is optically thick, the luminosity in the modulated component is independent of surface density, so that its fractional modulation decreases as the luminosity increases.

As we have discussed in section 5.3, there is also considerable uncertainty in H/r, even given a disk surface density. If the disk thickness and optical depth were determined by the considerations of conventional time-steady accretion flows around single black holes, the characteristic cooling time $\tau H/c$ can be identified with $(\alpha\Omega)^{-1}$. The fluctuation suppression factor could then be estimated by $\simeq 3\alpha\Omega/\omega$. Here the relevant orbital frequency is $\Omega(2.4a) = 0.26\Omega_{\rm bin}$, while $0.74\Omega_{\rm bin} \leq \omega \leq 1.46\Omega_{\rm bin}$ (the upper limit applies in the equal-mass case, the lower limit when the masses are very unequal). Thus, the suppression factor estimated in this way is $\simeq 0.1(\alpha/0.2)$ for equal black hole masses, rising to double that in the limit of very unequal masses. However, this estimate is made uncertain by the fact that the disk in the vicinity of the surface density peak is certainly *not* in a state of inflow equilibrium. In addition, just as for the other estimate, the association of the periodic modulation with the lump means that any estimate based on assumptions of axisymmetry likely underestimates the local optical depth.

Both estimates suggest that the modulation will be suppressed by at least a factor of several, but both are also subject to considerable uncertainty, making the actual outcome unclear. It is worth pointing out that in the event the modulation is detectable, the period of the modulation would allow an estimate of the binary orbital period. When the binary mass ratio is unity, the binary orbital frequency is 0.68 times the frequency of the modulation; as the mass ratio departs from unity, the binary orbital frequency should rise toward $\simeq 1.36$ times the modulation frequency.

Finally, we remark that our predictions of EM signals from circumbinary disks around merging black holes are complementary to those previously made (Bode et al. 2012) in two ways. In the previous work, the period of EM emission *began* when the binary separation shrank to $8M$; that is when our calculation *ends*. In addition, that effort expressly excluded the disk proper, which they defined as $r \geq 16M$; in our work, that is the location of the overwhelming majority of the emission. Our effort also differs from previous work in this area in that we explicitly include radiation losses in the gas's energy equation and also tie the rate of radiation directly to the instantaneous local thermodynamic state of the gas (albeit in only a formal way). In addition, our discussion of the observability of periodic modulation in the lightcurve takes into account possible suppression of the variation due to optical depth in the source.

6. SUMMARY

By describing the binary black hole spacetime at separations of tens of gravitational radii through the PN approximation, we have been able to simulate many orbits of fluid motion around such a system in fully relativistic MHD. In so doing, we have demonstrated that the qualitative properties of circumbinary disks in such a regime are well described by an extrapolation from their properties in the Newtonian limit: Matter piles up at $\simeq 2.5a$, while smaller radii are largely cleared of mass; nonetheless, accretion continues through the inner gap, albeit reduced by a factor of a few from the rate at which it is supplied at larger radii.

At the same time, however, we have also investigated the initial stages of strongly relativistic behavior in the form of the disk's response to binary orbital evolution by gravitational wave emission. By carrying the disk's evolution through the transition from the epoch in which its characteristic inflow time is short compared to the binary evolution timescale all the way to the epoch in which the binary evolves much faster than the disk, we have established the time at which the binary "runs away" from the disk, and more importantly, the degree to which it does so. This decoupling causes a drop in both the torque the binary exerts on the disk and in the disk luminosity. However, a sizable fraction of the accretion rate at large radius continues to makes its way to the binary throughout this period.

The binary separation at which this decoupling occurs is rather smaller than commonly estimated, largely because the internal stresses produced by MHD turbulence in the disk are considerably greater than typical applications of the α-model had guessed. The actual value of $a_{\rm dec}$ is sensitive to the disk's thermodynamics to the degree that the absolute level of the internal stresses are proportional to the disk's internal pressure. Because accretion continues, luminosity released when the accreting gas reaches the black holes may illuminate the disk and heat it. This sort of feedback has the potential to keep the disk's inflow rate high, self-consistently sustaining the accretion rate.

Given the sort of accretion rates associated with AGN, the inner regions of circumbinary disks around binary black holes with separations of tens of gravitational radii can be almost as bright as AGN, although there may be identifying alterations in the shapes of their optical/UV continua.

We have also shown that the work done on streams passing from the inner edge of the circumbinary disk through the evacuated gap around the binary is carried back to the disk and dissipated there. Because the disk generically develops a non-axisymmetric density distribution at $\simeq 2.5$ binary separations, the dissipation rate

is modulated periodically with $\sim 5\%$ fractional amplitude. In the right circumstances, this modulation might be detectable, although optical depth in the disk is likely to diminish its fractional amplitude, particularly when the accretion rate is high enough to make the system luminous. If this modulation can be detected, its period would provide an estimator of the binary's orbital frequency with factor of 2 accuracy.

A number of our results may be sensitive to the particular parameters chosen, most importantly equal masses in the binary, spinless black holes, and perfect alignment between the orientation of the binary's orbital angular momentum and the disk's angular momentum. Moreover, these choices can interact: for example, black hole spins oblique to the gas orbital plane can induce changes in that plane. Future work exploring a variety of choices for these parameters may reveal additional effects.

This work was supported by several NSF grants. S.C.N, M.C, and Y.Z. received support from AST-1028087 and J.H.K. from AST-1028111. M.C., B.C.M, H.N, Y.Z. also acknowledge partial support from PHY-0929114, PHY-0969855, PHY-0903782, OCI-0832606 and DRL-1136221. NY acknowledges support from NSF grant PHY-1114374 and NASA grant NNX11AI49G, under sub-award 00001944. We thank C. Lousto (RIT), John Hawley (UVa), K. Sorathia (JHU), J. Schnittman (Goddard) and Jiming Shi (UC Berkeley) for valuable discussions on the manuscript. Computational resources were provided by the Ranger system at the Texas Advance Computing Center (Teragrid allocation TG-PHY060027N), which is supported in part by the NSF, and by NewHorizons at Rochester Institute of Technology, which was supported by NSF grant No. PHY-0722703, DMS-0820923 and AST-1028087.

APPENDIX

HYDROSTATIONARY TORUS SOLUTIONS IN GENERAL AXISYMMETRIC SPACETIMES

Here, we describe a method for calculating axisymmetric non-magnetized gas distributions supported by pressure gradients and rotation within an axisymmetric spacetime. We will assume a general spacetime with Killing vectors $(\partial/\partial\phi)^a$ and $(\partial/\partial t)^a$ that can be expressed in the simple form (in coordinates similar to spherical Boyer-Lindquist coordinates):

$$g_{\mu\nu} = \begin{bmatrix} g_{tt} & 0 & 0 & g_{t\phi} \\ 0 & g_{rr} & 0 & 0 \\ 0 & 0 & g_{\theta\theta} & 0 \\ g_{t\phi} & 0 & 0 & g_{\phi\phi} \end{bmatrix} , \tag{A1}$$

which means that the inverse metric is

$$g^{\mu\nu} = \begin{bmatrix} -\frac{g_{\phi\phi}}{A} & 0 & 0 & \frac{g_{t\phi}}{A} \\ 0 & \frac{1}{g_{rr}} & 0 & 0 \\ 0 & 0 & \frac{1}{g_{\theta\theta}} & 0 \\ \frac{g_{t\phi}}{A} & 0 & 0 & -\frac{g_{tt}}{A} \end{bmatrix} . \tag{A2}$$

where $A = g_{t\phi}^2 - g_{tt}\, g_{\phi\phi}$. We have verified that the ϕ-average of our PN spacetime, $\hat{g}_{\mu\nu}$, has this form to within the accuracy of our PN procedure.

The initial state of the simulation consists of matter in axisymmetric hydrostatic equilibrium with a specific angular momentum profile, ℓ. We start from the discussion of De Villiers et al. (2003), which is based on Chakrabarti (1985) and other citations mentioned therein. The disk is centered about the equator of the black hole's spin; we will eventually assume that it is initially isentropic. The time-independent and axisymmetric Euler-Lagrange equations reduce, essentially, to

$$\frac{\partial_i h}{h} + \frac{1}{2} u_t^2 \partial_i u_t^{-2} - \frac{\Omega}{1-\ell\Omega}\partial_i \ell = 0 \,, \tag{A3}$$

where the angular frequency—$\Omega = u^\phi/u^t$—is not a simple function of the specific angular momentum—$\ell = -u_\phi/u_t$. The 4-velocity, u^μ, in our symmetry has zero components: $u^r = u^\theta = u_r = u_\theta = 0$. One can show, from the normalization condition $u_\mu u^\mu = -1$, that

$$u_t = -\left[-g^{tt} + 2\ell\, g^{t\phi} - \ell^2 g^{\phi\phi}\right]^{-1/2} , \tag{A4}$$

and

$$\Omega = \frac{g^{t\phi} - \ell\, g^{\phi\phi}}{g^{tt} - \ell\, g^{t\phi}} \,. \tag{A5}$$

The solutions assume that

$$\Omega = \eta\, \lambda^{-q} \,, \tag{A6}$$

where η and q are yet to be determined parameters, and λ is defined by

$$\begin{aligned}\lambda^2 &= \frac{\ell}{\Omega} \\ &= \ell\,\frac{g^{tt} - \ell\, g^{t\phi}}{g^{t\phi} - \ell\, g^{\phi\phi}}\,. \end{aligned} \tag{A7}$$

We can eliminate Ω from this system by combining equations (A6) and (A7) to yield a non-linear algebraic equation for $\ell = \ell(r,\theta)$ in terms of the metric:

$$R(\ell) = g^{t\phi}\left[\ell^2 + \lambda^2(\ell)\right] - g^{tt}\ell - g^{\phi\phi}\ell\,\lambda^2(\ell) = 0\,, \tag{A8}$$

where

$$\begin{aligned}\ell &= \Omega\,\lambda^2 \\ &= \eta\,\lambda^{2-q}\,, \end{aligned} \tag{A9}$$

or

$$\lambda = \left(\frac{\ell}{\eta}\right)^{1/(2-q)}\,. \tag{A10}$$

Also, we can show that

$$\begin{aligned}\Omega &= \eta^{-2/(q-2)}\;\ell^{q/(q-2)} \\ &\equiv k\,\ell^{\zeta}\,, \end{aligned} \tag{A11}$$

where $k = \eta^{-2/(q-2)}$ and $\zeta = q/\,(q-2)$.

Typically, one "solves" equation (A8) by approximating λ^2 with its Schwarzschild value: $\lambda^2 \simeq -g^{tt}/g^{\phi\phi}$ (De Villiers et al. 2003; Noble et al. 2009; Farris et al. 2011). For our ϕ-averaged spacetimes, the Schwarzschild approximation is not so good[7]. Therefore, we need a better solution. We can solve this equation to roundoff precision by using a Newton-Raphson scheme. To do so, we will need to know $\partial R(\ell)/\partial\ell$:

$$\frac{\partial R}{\partial \ell} = g^{t\phi}\left[2\,\ell + \frac{\partial\lambda^2}{\partial\ell}\right] - g^{tt} - g^{\phi\phi}\left[\lambda^2 + \ell\,\frac{\partial\lambda^2}{\partial\ell}\right]\,, \tag{A12}$$

where $\partial\lambda^2/\partial\ell = 2\lambda^2/[(2-q)\ell]$. Let us come back to equation (A3). A solution to this equation yields our disk solution. The solution process involves integrating it from the inner disk's edge — located at $r_{\rm in}$ — to a point within the disk:

$$\int_{h_{\rm in}}^{h}\frac{dh}{h} = -\frac{1}{2}\int_{u_{t\rm in}}^{u_t}\frac{d(u_t)^{-2}}{(u_t)^{-2}} + \int_{\ell_{\rm in}}^{\ell}\frac{k\,\ell^{\zeta}}{1-k\,\ell^{\zeta+1}}d\ell\,. \tag{A13}$$

With the boundary condition, $h_{\rm in} = h(r_{\rm in},\theta=\pi/2) = 1$, one can solve this integral equation for $h = h(r,\theta)$:

$$h = \frac{u_{t\rm in} f(\ell_{\rm in})}{u_t(r,\theta) f(\ell(r,\theta))}\,, \tag{A14}$$

where u_t is given by equation (A4), ℓ is found using Newton-Raphson on equation (A8), $\ell_{\rm in} = \ell(r_{\rm in},\pi/2)$ is a boundary value, and $f(\ell) \equiv \left|1 - k\,\ell^{\zeta+1}\right|^{1/(\zeta+1)}$.

We want a distribution that resembles a torus, which has a pressure maximum at some radius r_p, and has finite extent. The parameters $\{\ell_{\rm in}, q, \eta\}$ determine whether we get such a solution. We would like to replace one of the degrees of freedom with r_p, however, there is not a closed-form solution for r_p in terms of any of the original parameters. We know that the fluid attains the Keplerian angular momentum at the pressure maximum (r_p) as the pressure gradient must be zero there. It means that $\ell_{\rm in}$ should be super-Keplerian at the inner edge ($r_{\rm in}$), and $\ell_{\rm out}$ should be sub-Keplerian at the outer edge ($r_{\rm out}$). We therefore know that $\ell_{\rm in} > \ell_K(r_{\rm in})$, $\ell_{\rm out} < \ell_K(r_{\rm out})$, and $\ell_p = \ell_K(r_p)$, where ℓ_K is the Keplerian specific angular momentum (see the next section below). However, we only have two free parameters, and now have three constraints (if we specify all $\ell_{\rm in}, \ell_{\rm out}$ and ℓ_p). It may be possible to change equation (A9) to look like:

$$\ell = \eta\,(\lambda - \lambda_0)^{2-q}\,, \tag{A15}$$

and then find λ_0 with this third constraint. Using these three constraints, however, does not yield a closed-form solution for q, η, and λ_0. Therefore, another Newton-Raphson procedure would be required. Hence, we relax the constraint on $\ell_{\rm out} < \ell_K(r_{\rm out})$, and let $r_{\rm out}$ be a result of our procedure. Using $\lambda_0 = 0$, we find that

$$q = 2 - \frac{\log\left(\ell_{\rm in}/\ell_p\right)}{\log\left(\lambda_{\rm in}/\lambda_p\right)}\,, \tag{A16}$$

$$\eta = \frac{\ell_p}{\lambda_p^{2-q}}\,, \tag{A17}$$

where $\lambda_p = \lambda(\ell_p, r_p)$ and $\lambda_{\rm in} = \lambda(\ell_{\rm in}, r_{\rm in})$ given by equation (A7).

We follow the solution process based on one described in Chakrabarti (1985), and is the following:

[7] When using the approximate method, we found the disk to undergo a low frequency breathing mode that dominated the early evolution of the disk.

1. Chose values of $(r_{\rm in}, r_p, \ell_{\rm in})$, and derive q and η using equations (A16) and (A17);
2. Calculate λ (and then ℓ) at a new (r,θ) via Newton-Raphson (using equations (A8) and (A10)) close to the previous location, so that the old location's value can be used as a seed to the Newton iteration to successfully find a solution;
3. Calculate u_t via equation (A4) then h at (r,θ) via equation (A14);

The solution process progresses throughout (r,θ) space until the boundary of the disk is found, where $h(r,\theta)=1$. The path we take starts at $(r,\theta)=(r_{\rm in},\pi/2)$, moves in increasing r along the $\theta=\pi/2$ line, and we test to see if h is increasing. If h is not increasing at first, then we stop and try a different set of parameters. If h is increasing at first, we then proceed until the outer edge of the disk is reached; this radius is denoted as $r_{\rm out}$. Then, $\forall r \in [r_{\rm in}, r_{\rm out}]$, we start from the $\theta=\pi/2$ solution and proceed backward and forward in θ along constant r to find $h(r,\theta)$.

The initial torus solution used herein is parameterized by $\ell_{\rm in}=8.743$, $\eta=1.961$, $q=1.642$, $r_{\rm in}=3a_0=60M$, $r_p=5a_0=100M$, $r_{\rm out}=11.75a_0=235M$.

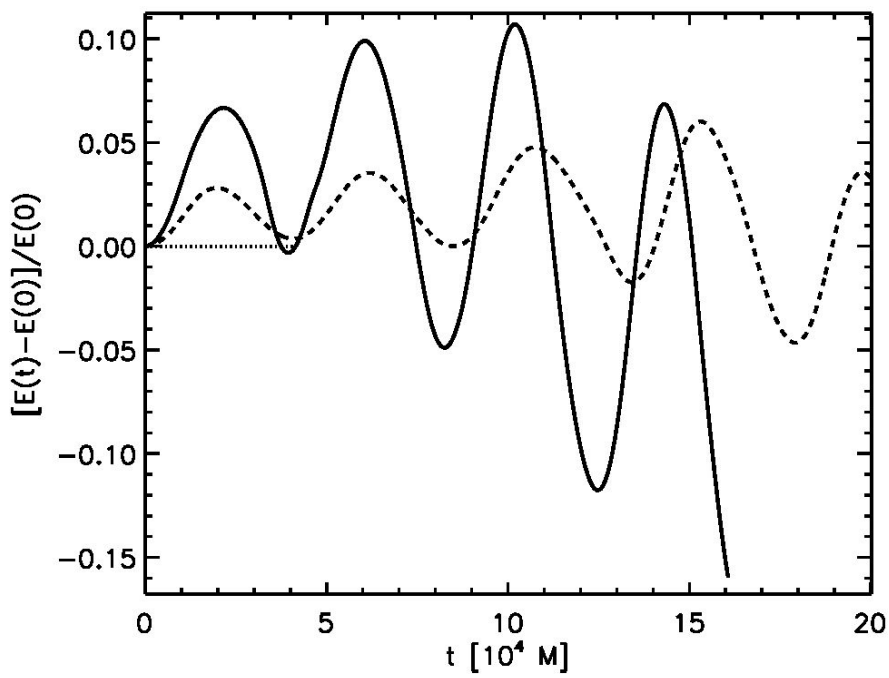

FIG. A1.— Change in total energy relative from its initial value versus time of non-magnetized tori from different runs. The first run used the so-called "approximate method" and was evolved in a PN BBH spacetime (solid); the second run used our new and more accurate procedure, but used the same spacetime as the first (dashes); the last used the same disk from the second run, but was evolved in the ϕ-average of the other runs' spacetime (dots). The curve for the last run (dots) oscillates with amplitude $\sim 10^{-8}$, which is why it appears consistent with zero in this figure. All the disks share the same parameters: $r_{\rm in}=2a_0$, $r_p=4a_0$, $a_0=30M$.

General Keplerian Velocity

The stationary torus solution described in Section A requires the Keplerian, or circular equatorial geodesic orbits, of the spacetime. Since we do not calculate $\hat{g}_{\mu\nu}$ in closed form, we require equations for these orbits based on a generalized metric of the form Equation (A1). Here, we state the equations governing the Keplerian orbits.

Keplerian orbits in our spacetime have 4-velocity, $u^\mu=[u^t,0,0,u^\phi]=u^t[1,0,0,\Omega_K]$. Ω_K is found from the r-component of the geodesic equation, $du^r/d\tau=-\Gamma^r{}_{\mu\nu}u^\mu u^\nu=0$, which ultimately yields

$$\begin{aligned}\Omega_{K\,\pm} &= \frac{1}{\Gamma^r{}_{\phi\phi}}\left[-\Gamma^r{}_{t\phi}\pm\sqrt{\left(\Gamma^r{}_{t\phi}\right)^2-\Gamma^r{}_{\phi\phi}\Gamma^r{}_{tt}}\right]\\ &= -\frac{1}{\partial_r g_{\phi\phi}}\left[\partial_r g_{t\phi}\pm\sqrt{\left(\partial_r g_{t\phi}\right)^2-\left(\partial_r g_{\phi\phi}\right)\left(\partial_r g_{tt}\right)}\right]\,. \end{aligned} \tag{A18}$$

$\Omega_{K\,-}$ and $\Omega_{K\,+}$ are the prograde angular velocity and retrograde angular velocity, respectively. The 4-velocity components are found by the normalization condition:

$$u^t = \left[g_{tt}+2\,\Omega\,g_{t\phi}+\Omega^2 g_{\phi\phi}\right]^{-1/2}\,, \tag{A19}$$

$$u^\phi = \Omega\,u^t\,. \tag{A20}$$

The Keplerian specific angular momentum, ℓ_K, is found by the relation between ℓ and Ω:

$$\ell = -\frac{g_{t\phi} + \Omega\, g_{\phi\phi}}{g_{tt} + \Omega\, g_{t\phi}} \,. \tag{A21}$$

RESOLUTION REQUIREMENTS

Our grid resolution was chosen to adequately resolve the MRI, to resolve the spiral density waves generated by the binary's potential, and to involve cells that are nearly cubical. We discuss each choice in turn.

Many recent studies have explored the resolution dependence of global MHD accretion disk simulations (Hawley et al. 2011; Sorathia et al. 2011; Shiokawa et al. 2012). Hawley et al. (2011) found that many global properties of the disk nearly asymptote with increasing resolution once the following criteria are satisfied:

$$N^{(z)} \gtrsim 16 \left(\frac{\beta}{100}\right)^{1/2} \left(\frac{\beta_z}{\beta}\right)^{1/2} \left(\frac{Q^{(z)}}{10}\right) , \tag{B1}$$

$$N^{(3)} \gtrsim 790 \left(\frac{0.1}{H/r}\right) \left(\frac{\beta}{10}\right)^{1/2} \left(\frac{Q^{(3)}}{25}\right) , \tag{B2}$$

where $N^{(z)}$ is the number of cells per scale height, H, $Q^{(z)} > 10$ is the recommended quality factor of the simulation, $\beta_z \equiv \langle p \rangle / \langle \left|\sqrt{g_{zz}} B^z\right|^2 \rangle$. We use spherical coordinates, so $N^{(\theta)}$ is needed instead:

$$N^{(z)} = \frac{H}{\Delta z} = \frac{H}{r\Delta\theta} = \frac{H/r}{\Delta\theta} \equiv N_{H/r} \quad , \tag{B3}$$

where $N_{H/r}$ is the number of cells in the poloidal direction per scale height. We see from prior simulations (e.g., Noble et al. (2010)) that $\beta \simeq 10$ and $\beta_z/\beta \simeq 50$ are reasonable for a disk in its asymptotic steady state, suggesting that $N_{H/r} > 36$. The initial condition values of $\beta \simeq 100$ and $\beta_z/\beta \simeq 1$, however, yield a weaker constraint ($N_{H/r} > 16$) on the resolution. Thus, we setup a grid such that $N_{H/r} \simeq 36$ with $H/r = 0.1$, our simulation's scale height. This is satisfied by the $x^{(2)}$ discretization described in Section 3.3. We also note that our condition satisfies the recommendation of $N_{H/r} > 32$ by Sorathia et al. (2011).

The more severe constraint is on the azimuthal symmetry. Both Hawley et al. (2011) and Sorathia et al. (2011) suggest that past simulations under-resolved the azimuthal direction and that one should cover the full azimuthal range $\phi \in [0, 2\pi]$ instead of assuming quarter- or half-circle symmetry. Since $\Delta\phi$ limits the time step size, we were only able to afford $N^{(3)} = 400$ as anything larger was impractical given our computational resources at the time. We were optimistic with this resolution, however, since the thinnest run of Noble et al. (2010) failed to satisfy Equation (B2) yet still resolved the MRI with $Q^{(3)} > 25$ throughout most of the disk's body.

We demonstrate how well RunIn and RunSS resolve the MRI in Figures B1 - B2, where we show mass-weighted averages of the $Q^{(2)}$ and $Q^{(3)}$ MRI quality factors:

$$Q^{(i)} = \frac{2\pi \left|b^i\right|}{\Delta x^{(i)}\, \Omega_K(r)\, \sqrt{\rho h + 2p_m}} \quad . \tag{B4}$$

The averages were made over $x^{(2)}$ in the following way:

$$\langle Q^{(i)} \rangle_\rho \equiv \frac{\int_0^1 Q^{(i)} \rho \sqrt{-g}\, dx^{(2)}}{\int_0^1 \rho \sqrt{-g}\, dx^{(2)}} \quad . \tag{B5}$$

A mass-weighting is used to calculate $\langle Q^i \rangle_\rho$ in order to bias the integral over the turbulent portion of the disk (the disk's bulk) rather than the laminar regions (e.g., corona, funnel). We find that the $Q^{(z)}$ constraint, i.e. $\langle Q^{(2)} \rangle_\rho > 10$, is satisfied for all times and regions in either RunIn or RunSS except for the densest parts of the lump at late times in RunSS . Similarly, the $Q^{(3)}$ constraint, i.e. $\langle Q^{(3)} \rangle_\rho > 25$, is satisfied for all times and regions in either RunIn or RunSS except for in the lump at late times in RunSS . We further note that $\langle B^r B_\phi \rangle / \langle p_m \rangle \simeq 0.3 - 0.35$ when averaged over the quasi-steady period of RunIn and RunSS ; this level is consistent with the asymptotic value found in resolution studies about point masses (Blackman et al. 2008; Guan et al. 2009; Davis et al. 2010; Simon et al. 2011; Hawley et al. 2011; Sorathia et al. 2011; Shiokawa et al. 2012).

We also aim to resolve the spiral density waves generated by the binary's time-dependent quadrupolar potential. This means that we need about ~ 10 cells per wavelength of the sound wave generated by the binary, $\lambda_d = 2\,\pi\, c_s/\Omega_{\rm bin}$, where $c_s = (H/r)\, r\, \Omega_K$ is the speed of sound. We use the Newtonian approximates $\Omega_{\rm bin} \simeq a^{-3/2}$ and $\Omega_K \simeq r^{-3/2}$ to simplify λ_d: $\lambda_d \simeq 2\pi\, (H/r)\, r\, (a/r)^{3/2}$. We want to resolve λ_d in ϕ and r out to r_p, which means that we want to satisfy another quality condition: $\lambda_d/\Delta r, \lambda_d/r\Delta\phi \simeq Q_d$, where Q_d will be the target number of cells per spiral density wavelength. Using the grid specifications described in Section 3.3, it is easy to show that the resolution constraints become:

$$N^{(1)} \simeq 305 \left(\frac{r_p/a_0}{5}\right)^{3/2} \left(\frac{0.1}{H/r}\right) \left(\frac{\ln\left(r_{\rm max}/r_{\rm min}\right)}{\ln\left(13/0.75\right)}\right) \left(\frac{Q_d}{6}\right) \quad , \tag{B6}$$

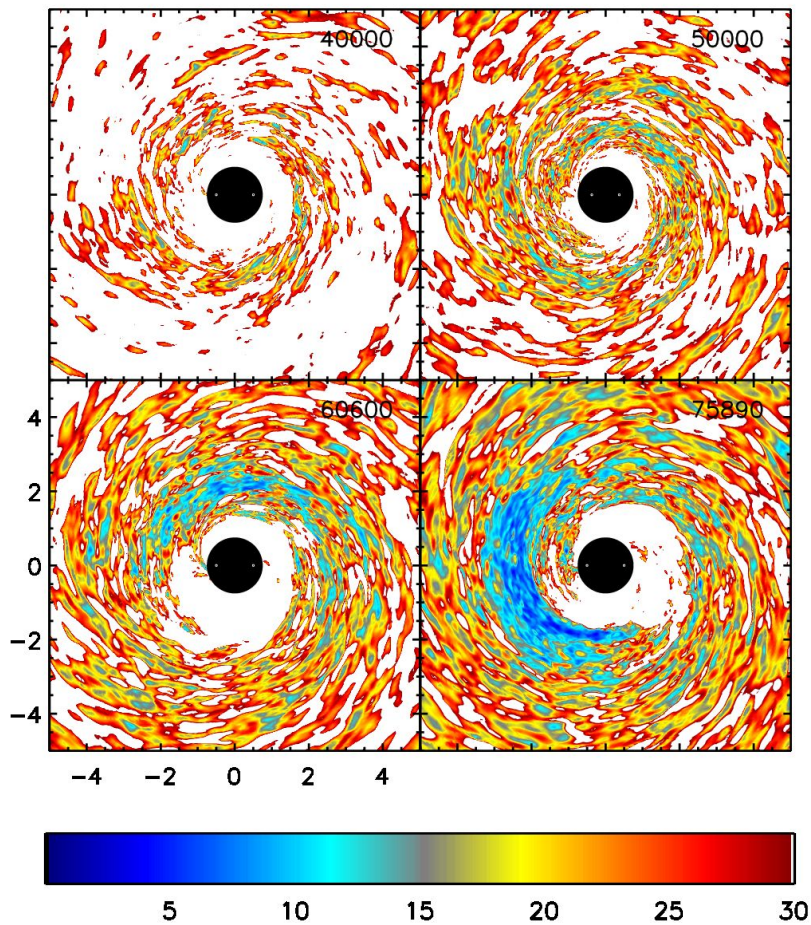

FIG. B1.— $\langle Q^{(2)} \rangle_\rho$ from RunIn (top row) and RunSS (second row) at late times in each simulation. The times of each snapshot are specified in the upper-right corner of each frame in units of M. The vertical and horizontal axes are in units of $a_0 = 20M$. We note that the $t = 40000M$ snapshot is shared by RunIn and RunSS . The color map used to make the snapshots is given in the bottom row.

$$N^{(3)} \simeq 671 \left(\frac{0.1}{H/r}\right) \left(\frac{r_p/a_0}{5}\right)^{3/2} \left(\frac{Q_d}{6}\right) \quad . \tag{B7}$$

We find that the spiral density wave criterion is stricter than the MRI criterion when

$$Q_d \left(\frac{r}{a}\right)^{3/2} > \beta^{1/2} Q^{(3)} \, . \tag{B8}$$

Again, we did not satisfy the constraint on azimuthal resolution with our choice of $N^{(3)} = 400$. In this case, we were reassured by evidence found by Shi et al. (2011) that found that the spiral density waves were extended over a large azimuthal extent and required far fewer cells than expected in that direction to resolve. In practice, we find that spiral density waves are short-lived as they propagate through the turbulent, shear flow of the disk; they are hardly ever seen in snapshots of intrinsic quantities past $r \simeq 3a_0$.

Since gridscale dissipation scales with the ratio of the cell extent to characteristic length scales of the physical quantities, cells that are oblate may effectively lead to anisotropic dissipation. Because physical dissipation mechanisms are isotropic, this effect could lead to unphysical artifacts. For this reason, we attempt to make the cells within the bulk of the disk—where most of the dissipation occurs—as isotropic as possible. Our runs use grids with $\Delta r : r\Delta\theta : r\Delta\phi :\simeq 3 : 1 : 3$ as measured in the $\theta = \pi/2$ plane. Sorathia et al. (2011) suggested that $\Delta r = r\Delta\phi$ and $\Delta\phi/\Delta\theta \leq 2$; we satisfy the former, and violate the latter by a slim margin: $\Delta\phi$ should be just 2/3 times the size we use. We note that the poloidal extent increases off the equator, so that the cells become more cubical at larger $|\theta - \pi/2|$.

MASS, ENERGY, AND ANGULAR MOMENTUM BUDGETS

Space and time gradients of the accretion flow's extensive quantities, mass (M), energy (E) and angular momentum (J) are fundamental for understanding the disk's evolution and structure. In stationary spacetimes, M, E, and J are all conserved. In our (t, ϕ)-dependent spacetime, E and J are no longer strictly conserved. We describe here how several functions used throughout the paper are derived from the evolution equations of mass, energy and angular momentum.

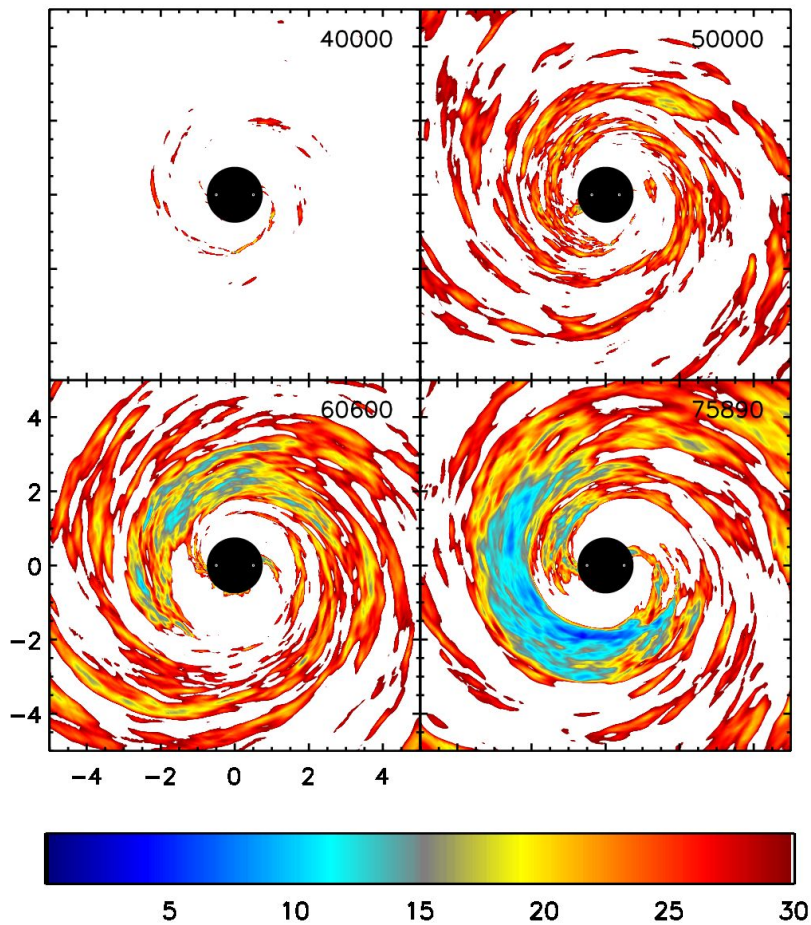

FIG. B2.— Same as in Figure B1, but for $\langle Q^{(3)}\rangle_\rho$.

Angular Momentum

We begin this section with the angular momentum equation because of its import to accretion physics. We follow the notation and derivation procedure outlined in Farris et al. (2011).

An extensive quantity, J, is the integral over the spatial volume of the time component of the its associated current, j^μ: $J = \int j^t \sqrt{-g}\, dV$, where dV is the spatial volume component in the spacelike hypersurface (e.g., $drd\theta d\phi$). We are interested in the azimuthal component of the momentum as that is the dominant component of the gas' and the binary's momenta. We therefore recognize that $j^\mu = T^\mu{}_\nu \phi^\nu$, and $\phi^\nu = (\partial_\phi)^\nu = \partial x^\nu/\partial\phi = [0,0,0,1]$ in spherical coordinates, which is what we use. We wish to calculate $d^2J/dtdr$. If J is locally conserved perfectly, $\nabla_\mu j^\mu = 0$. In our case it will not be conserved exactly, and exploring the radial gradient of its volume integral will help us understand how MHD stresses and the binary's gravitational torque compete over the run of the flow. This quantity is:

$$\begin{aligned}\frac{d}{dr}\int (\nabla_\mu j^\mu)\, \sqrt{-g}\, drd\theta d\phi &= \partial_r \int \left(\partial_\mu \sqrt{-g}\, j^\mu\right)\, drd\theta d\phi \\ &= \partial_r\partial_t J + \partial_r\partial_i \int j^i\, \sqrt{-g}\, drd\theta d\phi \\ &= \partial_r\partial_t J + \partial_r \int T^r{}_\phi\, \sqrt{-g}\, d\theta d\phi\,, \end{aligned} \tag{C1}$$

where the last equality results from the fact that j^θ is zero on the axis, and $j^\phi(\phi=0) = j^\phi(\phi=2\pi)$. On the other hand, we know from the stress-energy EOM—$\nabla_\mu T^\mu{}_\nu = -\mathcal{F}_\nu$—that

$$\begin{aligned}\frac{d}{dr}\int (\nabla_\mu j^\mu)\, \sqrt{-g}\, drd\theta d\phi &= \int (\nabla_\mu j^\mu)\, \sqrt{-g}\, d\theta d\phi \\ &= \frac{dT}{dr} - \int \mathcal{F}_\phi\, \sqrt{-g}\, d\theta d\phi\,, \end{aligned} \tag{C2}$$

where the torque density, dT/dr, can be expressed as

$$\frac{dT}{dr} = \int T^\mu{}_\nu \Gamma^\nu{}_{\mu\phi}\, \sqrt{-g}\, d\theta d\phi \;=\; \frac{1}{2}\int T^{\mu\nu}\partial_\phi g_{\mu\nu}\, \sqrt{-g}\, d\theta d\phi\,. \tag{C3}$$

We remind the reader that $\mathcal{F}_\nu$ is the radiative cooling flux (see Section 3 for details).

Therefore, equating the two equations (C1) and (C2), we have

$$\begin{aligned} \partial_r \partial_t J &= \frac{dT}{dr} - \{\mathcal{F}_\phi\} - \partial_r \{T^r{}_\phi\} \\ &= \frac{dT}{dr} - \{\mathcal{F}_\phi\} - \partial_r \{M^r{}_\phi\} - \partial_r \{R^r{}_\phi\} - \partial_r \{A^r{}_\phi\} \,, \end{aligned} \tag{C4}$$

where we have used here the shorthand

$$\{X\} \equiv \int \sqrt{-g}\, X d\theta\, d\phi \;= \langle X \rangle \int \sqrt{-g}\, d\theta\, d\phi \,. \tag{C5}$$

Also, $M^r{}_\phi$, $R^r{}_\phi$, and $A^r{}_\phi$ are—respectively—the Maxwell (MHD) stress, Reynolds stress, and advected flux of angular momentum. We note that $M^\mu{}_\nu = 2p_m u^\mu u_\nu + p_m \delta^\mu{}_\nu - b^\mu b_\nu$ is the EM part of $T^\mu{}_\nu$, while $(R^\mu{}_\nu + A^\mu{}_\nu) = T_H{}^\mu{}_\nu = \rho h u^\mu u_\nu + p\delta^\mu{}_\nu$ is the hydrodynamic part. The Reynolds stress alone is more complicated to calculate as we have to find the perturbation from the mean flow:

$$R^r{}_\phi = \rho h\, \delta u^r\, \delta u_\phi \,, \tag{C6}$$

where

$$\delta u^\mu \equiv u^\mu - \{\rho u^\mu\} / \{\rho\} \,. \tag{C7}$$

We note that we include the enthalpy as it technically contributes to the stress; its contribution is insignificant, however, for our relatively cool flow. The quantities $\{R^\mu{}_\nu\}$ and $\{A^\mu{}_\nu\}$ are not calculated during the simulation, but found approximately from other shell-integrated quantities we do calculate; $\{M^\mu{}_\nu\}$, $\{\mathcal{F}_\mu\}$, and dT/dr *are* calculated as stated above during the run. One can easily show from equations (C6) and (C7) that

$$\{R^r{}_\phi\} \;=\; \{\rho h\, \delta u^r\, \delta u_\phi\} \;\simeq\; \left\{T_H{}^r{}_\phi\right\} - \{A^r{}_\phi\} \tag{C8}$$

where $T_H{}^r{}_\phi$ is the hydrodynamic part of $T^r{}_\phi$, and $\{A^r{}_\phi\}$ is calculated approximately as

$$\{A^r{}_\phi\} \simeq \frac{\{\rho\ell\}\,\{\rho h u^r\}}{\{\rho\}} \,. \tag{C9}$$

Here, $\ell = -u_\phi/u_t$ as its defined in Appendix A. The approximations used to find equations (C8-C9) include: 1) $h \simeq 1$, and 2) $u_t \simeq -1$. We have demonstrated that these assumptions are valid to the few percent level in the bound portion of the flow for our simulations described in this paper.

Energy

Torques and stresses do work on the gas, transporting angular momentum. This work can be dissipated in the disk, changing its internal energy, which is eventually radiated away in part. Here we calculate the partitions in which the energy can move into; this calculation is nearly identical to that for $d^2J/dtdr$ in Appendix C.1 The current associated with E is $e^\mu = T^\mu{}_\nu t^\nu$, where t^μ is the 4-vector along time coordinate, $t^\mu = [1, 0, 0, 0]$. They are related by $E = \int e^t \sqrt{-g}\, dV$. Just as with j^μ, the divergence of e^μ is not exactly zero, because of the time-dependent spacetime. Using a similar analysis as before, we get

$$\partial_r \partial_t E \;=\; dW/dr \;-\; \{\mathcal{F}_t\} \;-\; \partial_r \{T^r{}_t\} \tag{C10}$$

where $dW/dr = \left\{\frac{1}{2} T^{\mu\nu} \partial_t g_{\mu\nu}\right\}$ is the work done by the spacetime on the matter.

Mass Accretion Rate

The current $j^\mu = \rho u^\mu$ is associated with the conserved quantity M, so we have $M = \int \rho u^t \sqrt{-g}\, dV$, and

$$\frac{dM}{dt} \;=\; -\int \rho u^r \sqrt{-g}\, d\theta d\phi \,. \tag{C11}$$

by using a similar technique to obtain Equation (C1).

REFERENCES

Ajith, P., Boyle, M., Brown, D. A., Brugmann, B., Buchman, L. T., et al. 2012

Alvi, K. 2000, Phys.Rev., D61, 124013

—. 2003, Phys.Rev., D67, 104006

Anninos, P., Fragile, P. C., & Salmonson, J. D. 2005, ApJ, 635, 723

Baker, J. G., Boggs, W. D., Centrella, J., Kelly, B. J., McWilliams, S. T., et al. 2007, Astrophys. J., 668, 1140

—. 2008, Astrophys. J., 682, L29

Baker, J. G., Centrella, J., Choi, D.-I., Koppitz, M., & van Meter, J. 2006, Phys. Rev. Lett., 96, 111102

Balbus, S. A., & Hawley, J. F. 1998, Reviews of Modern Physics, 70, 1

Barack, L. 2009, Class. Quant. Grav., 26, 213001

Bardeen, J. M., Bond, J. R., Kaiser, N., & Szalay, A. S. 1986, ApJ, 304, 15

Blackman, E. G., Penna, R. F., & Varnière, P. 2008, New A, 13, 244

Blanchet, L. 2002, Living Rev. Relativity, 5, 3

Blanchet, L. 2003, in 2001: A Relativistic Spacetime Odyssey, ed. I. Ciufolini, D. Dominici, & L. Lusanna, 411–430

Blanchet, L., Faye, G., & Ponsot, B. 1998, Phys. Rev., D58, 124002

Bode, T., Bogdanović, T., Haas, R., Healy, J., Laguna, P., & Shoemaker, D. 2012, ApJ, 744, 45

Bode, T., Haas, R., Bogdanović, T., Laguna, P., & Shoemaker, D. 2010, ApJ, 715, 1117

Bonning, E., Marronetti, P., Neilsen, D., & Matzner, R. 2003, Phys. Rev. D, 68, 044019
Campanelli, M., Lousto, C. O., Marronetti, P., & Zlochower, Y. 2006, Phys. Rev. Lett., 96, 111101
Campanelli, M., Lousto, C. O., Nakano, H., & Zlochower, Y. 2009, Phys. Rev. D, 79, 084010
Campanelli, M., Lousto, C. O., Zlochower, Y., & Merritt, D. 2007a, Astrophys. J., 659, L5
—. 2007b, Phys. Rev. Lett., 98, 231102
Chakrabarti, S. K. 1985, ApJ, 288, 1
Davis, M., Efstathiou, G., Frenk, C. S., & White, S. D. M. 1985, ApJ, 292, 371
Davis, S. W., Stone, J. M., & Pessah, M. E. 2010, ApJ, 713, 52
De Villiers, J.-P., & Hawley, J. F. 2003, ApJ, 592, 1060
De Villiers, J.-P., Hawley, J. F., & Krolik, J. H. 2003, ApJ, 599, 1238
Einstein, A. 1915, Sitzungsber. Preuss. Akad. Wiss. Berlin (Math. Phys.), 1915, 831
Farris, B. D., Liu, Y. T., & Shapiro, S. L. 2010, Phys. Rev. D, 81, 084008
—. 2011, Phys. Rev. D, 84, 024024
Gammie, C. F., McKinney, J. C., & Tóth, G. 2003, ApJ, 589, 444
Giacomazzo, B., Baker, J. G., Miller, M. C., Reynolds, C. S., & van Meter, J. R. 2012, ArXiv e-prints
González, J. A., Hannam, M. D., Sperhake, U., Brugmann, B., & Husa, S. 2007, Phys. Rev. Lett., 98, 231101
Guan, X., Gammie, C. F., Simon, J. B., & Johnson, B. M. 2009, ApJ, 694, 1010
Gültekin, K., et al. 2009, ApJ, 698, 198
Hawley, J. F., Guan, X., & Krolik, J. H. 2011, ApJ, 738, 84
Healy, J., et al. 2009, Phys. Rev. Lett., 102, 041101
Herrmann, F., Hinder, I., Shoemaker, D., Laguna, P., & Matzner, R. A. 2007, Astrophys. J., 661, 430
Hinder, I., Herrmann, F., Laguna, P., & Shoemaker, D. M. 2010, Phys. Rev., D82, 024033
Hinder, I., Vaishnav, B., Herrmann, F., Shoemaker, D. M., & Laguna, P. 2008, Phys. Rev., D77, 081502
Hirose, S., Blaes, O., & Krolik, J. H. 2009, ApJ, 704, 781
Hughes, S. A. 2009, Ann. Rev. Astron. Astrophys., 47, 107
Jennrich, O. 2009, Classical and Quantum Gravity, 26, 153001
Johnson-McDaniel, N. K., Yunes, N., Tichy, W., & Owen, B. J. 2009, Phys. Rev., D80, 124039
Kelly, B. J., Tichy, W., Campanelli, M., & Whiting, B. F. 2007, Phys. Rev., D76, 024008
Kelly, B. J., Tichy, W., Zlochower, Y., Campanelli, M., & Whiting, B. F. 2010, Class. Quant. Grav., 27, 114005
Kocsis, B., Yunes, N., & Loeb, A. 2011, Phys. Rev., D84, 024032
Koide, S., Shibata, K., & Kudoh, T. 1999, ApJ, 522, 727
Komissarov, S. S. 2005, MNRAS, 359, 801
Koppitz, M., Pollney, D., Reisswig, C., Rezzolla, L., Thornburg, J., et al. 2007, Phys. Rev. Lett., 99, 041102
Krolik, J. H. 1999, Active galactic nuclei : from the central black hole to the galactic environment (Princeton University Press)
—. 2010, ApJ, 709, 774
Krolik, J. H., Hawley, J. F., & Hirose, S. 2005, ApJ, 622, 1008
Kylafis, N. D., & Klimis, G. S. 1987, ApJ, 323, 678
Liu, Y. T., & Shapiro, S. L. 2010, Phys. Rev. D, 82, 123011
Lousto, C. O., Nakano, H., Zlochower, Y., & Campanelli, M. 2010, Phys. Rev., D81, 084023
Lousto, C. O., & Zlochower, Y. 2011, Phys. Rev. Lett., 107, 231102
Lousto, C. O., Zlochower, Y., Dotti, M., & Volonteri, M. 2012
MacFadyen, A. I., & Milosavljević, M. 2008, ApJ, 672, 83
Milosavljević, M., & Phinney, E. S. 2005, ApJ, 622, L93
Mino, Y., Sasaki, M., Shibata, M., Tagoshi, H., & Tanaka, T. 1997, Prog. Theor. Phys. Suppl., 128, 1
Mora, T., & Will, C. M. 2004, Phys. Rev., D69, 104021
Mundim, B. C., Kelly, B. J., Zlochower, Y., Nakano, H., & Campanelli, M. 2011, Class. Quant. Grav., 28, 134003
Nelson, R. P., & Papaloizou, J. C. B. 2003, MNRAS, 339, 993
Noble, S. C., Gammie, C. F., McKinney, J. C., & Del Zanna, L. 2006, ApJ, 641, 626
Noble, S. C., Krolik, J. H., & Hawley, J. F. 2009, ApJ, 692, 411
—. 2010, ApJ, 711, 959
Palenzuela, C., Anderson, M., Lehner, L., Liebling, S. L., & Neilsen, D. 2009, Physical Review Letters, 103, 081101
Palenzuela, C., Garrett, T., Lehner, L., & Liebling, S. L. 2010a, Phys. Rev. D, 82, 044045
Palenzuela, C., Lehner, L., & Liebling, S. L. 2010b, Science, 329, 927
Papaloizou, J. C. B., & Nelson, R. P. 2003, MNRAS, 339, 983
Penna, R. F., McKinney, J. C., Narayan, R., Tchekhovskoy, A., Shafee, R., & McClintock, J. E. 2010, MNRAS, 408, 752
Peters, P. C. 1964, Phys. Rev., 136, B1224
Poisson, E. 1995, Phys. Rev., D52, 5719
Poisson, E., Pound, A., & Vega, I. 2011, Living Rev. Relativity, 14, 7
Pretorius, F. 2005, Phys. Rev. Lett., 95, 121101
Pringle, J. E. 1991, MNRAS, 248, 754
Sasaki, M., & Tagoshi, H. 2003, Living Rev. Relativity, 6, 6
Sathyaprakash, B. S., & Schutz, B. F. 2009, Living Rev. Relativity, 12, 2
Scheel, M. A., et al. 2006, Phys. Rev., D74, 104006
Schwarzschild, K. 1916, Sitzunsber. Dtsch. Akad. Wiss Berlin, Kl. Math. Phys. Tech.
Shakura, N. I., & Sunyaev, R. A. 1973, A&A, 24, 337
Shi, J.-M., Krolik, J. H., Lubow, S. H., & Hawley, J. F. 2011, ArXiv e-prints
Shiokawa, H., Dolence, J. C., Gammie, C. F., & Noble, S. C. 2012, ApJ, 744, 187
Simon, J. B., Hawley, J. F., & Beckwith, K. 2011, ApJ, 730, 94
Simone, L. E., Leonard, S. W., Poisson, E., & Will, C. M. 1997, Class. Quant. Grav., 14, 237
Sorathia, K. A., Reynolds, C. S., Stone, J. M., & Beckwith, K. 2011, ArXiv e-prints
Sperhake, U., Berti, E., Cardoso, V., González, J. A., Brügmann, B., & Ansorg, M. 2008, Phys. Rev., D78, 064069
Tanaka, T., & Menou, K. 2010, ApJ, 714, 404
Tchekhovskoy, A., McKinney, J. C., & Narayan, R. 2007, MNRAS, 379, 469
Thorne, K. S. 1980, Rev. Mod. Phys., 52, 299
Tichy, W., Bruegmann, B., Campanelli, M., & Diener, P. 2003, Phys. Rev., D67, 064008
Tóth, G. 2000, Journal of Computational Physics, 161, 605
Weisberg, J. M., & Taylor, J. H. 2005, ASP Conf. Ser., 328, 25
Wen, Z. L., Jenet, F. A., Yardley, D., Hobbs, G. B., & Manchester, R. N. 2011, ApJ, 730, 29
Will, C. M. 2011, Proc. Nat. Acad. Sci., 108, 5938
Winters, W. F., Balbus, S. A., & Hawley, J. F. 2003, ApJ, 589, 543
Yunes, N. 2007, Class. Quant. Grav., 24, 4313
Yunes, N., & Berti, E. 2008, Phys. Rev., D77, 124006
Yunes, N., Kocsis, B., Loeb, A., & Haiman, Z. 2011, Phys. Rev. Lett., 107, 171103
Yunes, N., & Tichy, W. 2006, Phys. Rev., D74, 064013
Yunes, N., Tichy, W., Owen, B. J., & Bruegmann, B. 2006, Phys. Rev., D74, 104011
Zhang, Z., Yunes, N., & Berti, E. 2011, Phys. Rev., D84, 024029